The Notch1/Delta-like-4 axis is crucial for the initiation and progression of oral squamous cell carcinoma

Christian T. Meisel[1], Riccardo Destefani[1], Ilaria J. Valookkaran[1], Niels Rupp[2], Aashil Batavia[2], Francesca Catto[3], Jacqueline Hofmann-Lobsiger[1], Thimios A. Mitsiadis[1], Cristina Porcheri[1*]

[1] Institute of Oral Biology, Faculty of Medicine, University of Zurich, Plattenstrasse 11, 8032 Zurich, Switzerland

[2] Department of Pathology and Molecular Pathology, University Hospital Zurich, Rämistrasse 100, 8091 Zurich, Switzerland

[3] IMAI-MedTech, Bio-technopark, Wagistrasse 18, 8952 Schlieren, Switzerland

* Correspondence: cristina.porcheri@zzm.uzh.ch

Abstract

The Notch signaling pathway is frequently altered in Oral Squamous Cell Carcinoma (OSCC), the most common malignant neoplasm of the oral mucosa. In this study, we aimed to elucidate the functional role of this pathway in OSCC initiation and progression. Using transgenic animal models, advanced imaging, and next-generation-sequencing techniques, we analyzed Notch-dependent changes driving OSCC. We found specific expression patterns of Notch1 and Delta-like-4 confined to the malignant tissue, while Jagged1 was downregulated in OSCC. This mutually exclusive expression of Delta-like-4 and Jagged1 occurs at the early hyperplastic stage and persists until more advanced stages of the tumor. Transcriptomic analyses confirmed the dysregulation of the Notch pathway circuitry associated with a genetic signature for undifferentiation in OSCC. Furthermore, pharmacological Notch inhibition significantly impaired cancer cell motility. Taken

25 together, these results reveal the pivotal importance of the Notch1/Delta-like-4 signaling axis as a
26 central oncogenic driver in OSCC.
27
28 **Keywords**
29 Notch signaling pathway, oral cancers, squamous cell carcinoma, OSCC, keratinocyte
30 differentiation, Notch inhibitors, Notch ligands, Delta-like-4, Notch1, Jagged1
31
32
33

34 **List of abbreviations**

35 4NQO – 4-nitroquinoline-1-oxide
36 CSL – CBF, Suppressor of Hairless, Lag-1
37 Dll4 – Delta-like-4
38 DMSO – Dimethyl sulfoxide
39 E-Cad – E-cadherin
40 EMT – Epithelial-to-mesenchymal-transition
41 GFP – Green fluorescent protein
42 GO – Gene Ontology
43 GSEA – Gene set enrichment analysis
44 Hes – Hairy and enhancer of split-1
45 Hey – Hairy and enhancer of split related with YPRW motif protein
46 HNSCC – Head and neck squamous cell carcinoma
47 Jag1 – Jagged1
48 K5/10/14 – Keratin 5/10/14
49 MesoSPIM – Mesoscale selective plane illumination microscopy
50 OSCC – Oral squamous cell carcinoma
51 RBPj – Recombining binding protein suppressor of hairless
52 Runx1 – Runt-related transcription factor 1
53 Sox2 – SRY-Box Transcription Factor 2
54 TAM – Tamoxifen
55

56 **Main**

57

58 Head and neck squamous cell carcinoma (HNSCC) is the sixth most common type of cancer,
59 annually affecting 850.000 people worldwide [1–3]. Although modern multimodal therapy has
60 improved clinical management of this disease, tumor recurrence and distal metastasis correlate
61 with a poor prognosis, with a median overall survival of ten months [4,5]. HNSCC regroups a variety
62 of cancers arising from the oral mucosa, nasal cavities, pharynx, and larynx, which have their own
63 unique carcinogenic evolution and clinical score [6].

64 In normal mucosal tissues, such as the oral and respiratory epithelia, keratinocytes undergo a well-
65 defined differentiation process as they move from the basal layer to the surface. In the basal layer,
66 stem-cell-like cells express undifferentiated markers such as SRY-box transcription factor 2
67 (SOX2), P63, and Keratin 5 and 14 (K5, K14). As these cells progress upward they begin to
68 differentiate, producing keratins and junctional and structural proteins essential for the formation
69 of the mucosal barrier [7]. In SCC, the normal keratinocyte differentiation process is disrupted,
70 leading to uncontrolled proliferation and impaired differentiation [8]. Basal keratinocytes bypass
71 typical differentiation stages and continue to proliferate in an undifferentiated or partially
72 differentiated state. This results in the accumulation of abnormal, poorly differentiated cells that
73 resist cell death and shedding.

74 Within tumors, cancer-initiating cells retain self-renewal capabilities, driving tumor initiation and
75 exhibiting resistance to conventional therapies [9]. These cells share undifferentiated markers with
76 epithelial stem cells, while the expression of keratins indicative of terminally differentiated
77 squamous cells (e.g., K10) is reduced or altered, reflecting the dedifferentiation character of tumor
78 cells.

79 Oral Squamous Cell Carcinoma (OSCC) originates from the mucosa of the oral cavity, with the
80 tongue being the most commonly affected site. OSCC develops progressively, starting with local
81 hyperplasia of squamous epithelial cells and advancing through dysplastic and invasive stages [10,3].
82 In squamous dysplasia, clusters of basaloid nonkeratinizing and poorly differentiated cells grow
83 on the epithelial surface as exophytic growth (e.i. Carcinoma in Situ) [11]. Aberrant epithelial cells
84 may infiltrate the neighboring muscles and spread along the mesenchymal lines to metastasize to
85 cervical lymph nodes [4,8]. Proximal metastases occur in up to 50% of patients and are associated
86 with the recurrence and development of distant metastases [6,12,13]. OSCC onset often relates to
87 chronic exposure to nitrosamines, polycyclic aromatic hydrocarbons, and other genotoxic
88 compounds (e.g. quinoline derivatives, arylamines), which in turn leads to genetic instability and
89 the dysregulation of the DNA repair process[10]. Clones with acquired genetic alterations have an
90 initial growth advantage and can potentially transform into aggressive subclones in the more
91 advanced stages of the disease [14,15,16]. High-risk premalignant lesions can be subtle, and timely
92 recognition relies on the detection of stage-specific molecular biomarkers.
93 Mutational profiling consistently identified chromosomal alterations resulting in the amplification
94 of *cyclin D1* and EGFR regions, while genetic mutations affecting tongue epithelium have been
95 mapped in cyclin-dependent kinase inhibitor 2A (CDKN2A), tumor protein 53 (TP53) [3,17,18].
96 Notably, the Notch signaling pathway is one of the major mutation hotspots in OSCC[19–21]. Exome
97 sequencing screenings revealed that approximately 15% of tumors harbor mutations in this
98 pathway, including truncations, insertions-deletions, and missense variants.
99 Notch signaling is an evolutionary conserved pathway involved in cell fate specification and
100 differentiation [22]. It plays a crucial role in maintaining epithelial integrity, particularly in the oral
101 cavity, where it regulates mucosal formation and homeostasis from embryonic development

102 onward [22–27]. In mammals, four Notch receptors (Notch1-4) and five Notch-ligands (Jagged1,2 and
103 Delta-like-1,3,4) have been identified [28,29]. Upon receptor-ligand binding, a series of cleavages
104 take place to ultimately release the Notch intracellular domain (NICD), which then translocates
105 into the nucleus and acts as a transcription factor in a complex with CSL (also known as RBPj)
106 [22,30]. The activity of Notch is strictly context-dependent, therefore spatial distribution of each
107 receptor, ligand and downstream targets reflects in a distinct modulation of the pathway, hence
108 influencing tissue homeostasis [31]. Dysregulation of Notch signaling is found in several human
109 pathologies, and novel therapeutic approaches have been developed in recent years to specifically
110 target Notch components [31,32]. Although frequently mutated in OSCC[19–21], the precise role of
111 Notch in the initiation and development of this malignancy remains largely unknown, with
112 contrasting results that are supportive of either an oncogenic or a tumor-suppressive role [33–37].
113 Using *ad hoc* murine models, we have explored the functional role of Notch signaling in the
114 progression of OSCC, from initiation to the most advanced aggressive stages. Our findings reveal
115 a mutually exclusive expression of Dll4 and Jag1 that is consistently maintained across all stages
116 of tumor growth, from precancerous lesions to advanced invasive forms. Transcriptomic analysis
117 further confirmed the downregulation of Notch-specific target genes, alongside dysregulation of
118 genes involved in keratinocyte differentiation and cell-to-cell and cell-to-extracellular matrix
119 (ECM) communication. In parallel, pharmacological modulation of Notch-specific transcription
120 in human cancer cells led to a reduction in the malignant phenotype. Together, our data underscore
121 the critical role of the Notch1/Dll4 signaling axis in OSCC initiation and progression and
122 substantiate its suitability as both an early diagnostic tool and a functional target for OSCC
123 treatment.

124 **Materials and Methods**

125

126 **Animals**

127 C57Bl/6 and *Notch1*^{CreERT}*:R26mTmG*$^{fl/fl}$ mice were used for this study [38,39],The mice were
128 maintained and handled according to the Swiss Animal Welfare Law. This study was approved by
129 the Cantonal Veterinary office, Zurich (License ZH197/2017 and ZH086/2021).

130

131 **4NQO treatment of mice – OSCC murine model**

132 For the induction of OSCC, treated mice received drinking water containing 50µg/mL 4NQO
133 (#N8141, Sigma-Aldrich) starting at week 6 until week 22 of age. Control mice were littermates
134 receiving drinking water containing the same volume of DMSO (#D4540, Sigma-Aldrich). The
135 drinking solution was renewed twice a week. Females and males were equally represented in the
136 experimental set-up. After 16 weeks mice were either euthanized (time point 22 weeks) or given
137 normal drinking water until euthanasia (time point 32 weeks or 38 weeks). For lineage tracing
138 Notch1-driven expression, Cre was activated by the intraperitoneal injection of tamoxifen
139 50mg/kg dissolved in corn oil/10% EtOH (Sigma-Aldrich Cat#T5648) for two consecutive days.
140 All analyses were conducted in groups of 3 to 5 mice ($n \geq 3$).

141

142 **Sample embedding and cryo-sectioning**

143 After tissue isolation, samples were post fixed in 4% Paraformaldehyde (PFA) for 1h at 4°C and
144 cryopreserved in 30% sucrose. Tissues were embedded in a cryo-embedding matrix (Tissue-Tek,
145 O.C.T Compound, Sakura) and stored at -80°C until sectioning. Samples were sectioned (10µm)
146 in the cryostat (Leica CM3050S) and stored at -80°C until staining.

147

148 **Hematoxylin & Eosin staining**

149 Sections were washed for 3x5min in 1x PBS. Nuclei were stained with Hematoxylin for 20 seconds
150 (Sigma-Aldrich #51275). Cytoplasm was then stained with Eosin for 10 seconds (Sigma-Aldrich
151 #HT110216), thoroughly washed and mounted for imaging. Images were acquired using the Leica
152 DMC5400 microscope.

153

154 **Immunostaining of cryosections**

155 Immunofluorescence staining of cryosections was performed as previously described[40]. Briefly,
156 Cryosections (10–25 µm thick) were post-fixed with 4% PFA and permeabilized with a 0.5%
157 Triton/PBS solution for 30 minutes at room temperature. To minimize nonspecific antibody
158 binding, slides were then incubated for 1 hour at RT in a blocking buffer containing species-
159 specific serum and 0.1% Triton in PBS. Primary antibodies were diluted in the blocking buffer at
160 the following concentrations: polyclonal rabbit anti-Keratin14 (1:100; Poly19053, Biolegend),
161 polyclonal goat anti-E-Cadherin (1:200, AF748, R&D Systems), polyclonal goat anti-GFP (1:100;
162 ab6673; Abcam), polyclonal rabbit anti-DLL4 (1:100; ab7280; Abcam), polyclonal goat anti-
163 DLL4 (1:50; AF1389; R&D) polyclonal rabbit anti-Jag1 (1:100; ab7771; Abcam), polyclonal
164 rabbit anti-Keratin10 (1:100; PRB-159P; Biolegend), polyclonal Rabbit anti-Keratin5 (dilution
165 1:100; ab64081; Abcam) polyclonal rabbit anti-Notch1 (D1E11) (dilution 1:100; 3608S; Cell
166 Signaling), polyclonal rabbit anti-Runx1 (dilution 1:100; HPA004176; Atlas Antibodies),
167 polyclonal rabbit anti-p63 (dilution 1:100; ab53039; Abcam), monoclonal rabbit anti-Vimentin
168 (dilution 1:100; ab92547; Abcam), mouse anti-Snail (1:100, #14-9859-80 Invitrogen). Used
169 secondary antibodies: Goat anti-Rabbit IgG 488, Alexa Fluor Plus 488 (dilution 1:1000; A32731,

170 Invitrogen), goat anti-mouse IgG 647, Alexa Fluor Plus 647 (dilution 1:1000; A32728, Invitrogen),
171 donkey anti-Goat IgG 488, Alexa Fluor Plus 488 (dilution 1:1000; A32814; Invitrogen); donkey
172 anti-Rabbit IgG 647, Alexa Fluor 647 (dilution 1:1000; A32795: Invitrogen), streptavidin Alexa
173 Fluor 488 (dilution 1:100; S11223; Invitrogen). Nuclear counterstaining was performed using
174 DAPI (4',6-Diamidino-2-Phenylindole, Dihydrochloride, #D1306, Invitrogen).
175
176 **Image acquisition – Confocal microscopy**
177 Immunofluorescence images of the tongue tissue were produced using a Leica DM6000B
178 microscope, or Confocal Leica SP5/ SP8 with the following settings: 1024x1024 pixel dimension;
179 400Hz laser; frame average 3 or 4. photomultipliers PMT or Hyd. Fluorochromes used: Alexa 488,
180 546, 594, 647. A range of 10µm (standard) to 70µm (whole mount) thick Z-stack was analyzed
181 collecting images every 2µm (standard) or 10µm (whole mount). Images were processed using
182 Imaris 9.9 software (Bitplane). Photomerge Script from Photoshop (Adobe, Version 23.0.2) was
183 used for overview images reconstruction.
184
185 **Tissue clearance**
186 The separated epithelial sheet was embedded in 2% low-melting agarose. The tissue was then
187 transferred into Histodenz (#D2158, Sigma-Aldrich), dissolved in PBS1X and diluted until a
188 measurable refractive index of 1.457 for tissue clearance.
189
190 **Whole-organ 3D imaging**
191 Whole tongue images were recorded with a custom-made selective plane illumination microscope
192 (mesoSPIM) [41]. SPIM imaging was done after clearing and refractive index matching. The

193 laser/filter combinations for mesoSPIM imaging were as follows: for Notch1-GFP at 488 nm
194 excitation, a 405-488-561-640 nm QuadrupleBlock bandpass filter was used as the emission filter;
195 for membrane localized dt-Tomato at 561 nm excitation, a 561 nm long pass filter was used.
196 Transparent tongue epithelial whole-mount was imaged at a voxel size of 3.26 × 3.26 × 3 µm (X
197 × Y × Z). Further technical details of the mesoSPIM have been previously reported [41]
198 (*mesoSPIM.org*).
199

200 **Enzymatic separation of keratinized epithelium from mesenchyme of the murine tongue**
201 Separation was performed as previously described [42]. In brief, an enzymatic cocktail of collagenase
202 A (1mg/mL; Roche) and Dispase II (2mg/mL; #D4693 Sigma-Aldrich;) in 0.1 M PBS1X was
203 injected into the subepithelial space from the posterior cutting end of the tongue. Upon incubation
204 at 37°C for 30 min the mesenchyme and epithelium were pulled in opposing directions until
205 complete separation is achieved.

206 **Oral mucosal organoid establishment and treatment**

207 Oral mucosal organoids were established and propagated as previously described [43]. Briefly,
208 following enzymatic separation of the tongue epithelium, a keratinocyte cell suspension was
209 obtained and cultured in Advanced DMEM^{+++} supplemented with B27 (Life Technologies,
210 #17504-044), 1.25 mmol/L N-acetyl-L-cysteine and 10 mmol/L nicotinamide. Every three days
211 freshly prepared mRSPO1 (100 ng/mL, PeproTech), mEGF (50 ng/mL,) , and 10 ng/mL FGF10
212 was added. Organoids were passaged every 8 days by dissociating them into single cells using a
213 combination of trypsin digestion and mechanical disruption via pipetting. Trypsin was inactivated
214 using 10% FBS for 10 minutes at 37 °C, after which cells were centrifuged and resuspended in

215 complete organoid medium with growth factors. For treatment, either CB103 (100 µM;
216 MedChemExpress, #HY-135145) or an equivalent volume of DMSO (Sigma-Aldrich, #D8418)
217 was added to the organoid medium. Treated single cells were imaged every day, and organoid size
218 was quantified using FIJI/ImageJ software. Quantitative analyses were performed on 40 organoids
219 per condition.

220 **RNA isolation epithelial tissue**

221 Separated epithelial sheets were snap-frozen with liquid nitrogen and homogenized on ice for 3min
222 using a motor driven grinder (Pellet Pestle Motor, Kontes). Further isolation according to
223 manufacturer's instructions (RNeasy Mini Kit; Qiagen). Quantification of the total RNA extracted
224 by NanoDrop (Thermo Fischer Scientific, Waltham, USA). RNA was retrotranscribed using the
225 iScript™cDNA synthesis kit (Bio-Rad Laboratories AG, Cressier FR, Switzerland) according to
226 manufacturer's instructions.
227

228 **Quantitative real-time PCR**

229 The quantitative real-time PCR was performed using the CFX Connect Real-Time System and the
230 software CFX Manager Version 3.1. Expression level analysis of *Actin* (housekeeping gene), and
231 all candidate genes were performed using the SYBR® Green PCR Master Mix (Applied
232 Biosystems, Carlsbad CA, USA) in combination with corresponding oligonucleotide primers
233 (Supplementary Table 1 and 2).
234 All amplifications were done in technical duplicates of 5 biological replicates. Using the following
235 thermocycling conditions: 95°C for 10min; 40 cycles of 95°C for 15sec; 60°C for 60sec. Melting
236 curve analysis was performed at 95°C for 15sec, 60°C for 5sec and 95°C for 30sec. Expression

237 levels were calculated using the ΔΔCt method ($2^{-\Delta\Delta Ct}$ formula), after being normalized to the Ct-
238 value of the *Actin* housekeeping gene.
239
240 **Bioinformatic analysis**
241 Library for bulk seqRNA was prepared using Illumina NovaSeq 6000. Differentially expressed
242 genes were obtained from the DEseq2 output (p.adj <= 0.05) (Supplementary Method 1 and
243 Supplementary Method 2). We determine pathway enrichment using the ReactomePA v1.38.0
244 package [44]. We produce a similarity matrix using the Jaccard distance between the enriched terms
245 needed to produce the enrichment map using the R package enrichplot v1.14.1.
246 Raw data available on NCBI/SRA database (https://www.ncbi.nlm.nih.gov/sra/PRJNA1067290
247 and https://www.ncbi.nlm.nih.gov/sra/PRJNA1187878).
248
249 **Patients' samples**
250 Samples from patients diagnosed with HPV-negative HNSCC were used under the license BASEC
251 2018-01729. Tissues from patients 18-90 years old with primary tumor occurrence were collected
252 upon primary surgical therapy performed at the University Hospital Zurich (USZ). Tissues were
253 processed, embedded in OCT and sectioned according to USZ SOPs. For immunohistochemistry
254 staining, primary antibody α-Jagged1 (1:100; Abcam, ab7771) and α-Dll4 (1:100; R&D Systems,
255 AF1389) were used.
256
257 **Cell culture**
258 The SCC-25 epithelial cell line, derived from the tongue of a 70 years-old OSCC patient, was
259 purchased from the ATCC/LGC company (SCC-25CRL-1628™) and maintained accordingly to

260 producer indications. Briefly, cells were cultured in DMEM/F12 medium containing 1.2 g/L
261 sodium bicarbonate, 2.5 mM L-glutamine, 15 mM HEPES, 0.5 mM sodium pyruvate (# 11330032,
262 Gibco-ThermoFisher) and 10% fetal bovine serum (#16000044, Gibco-ThermoFisher). Cells were
263 sub-cultured when 80% confluent using trypsin/EDTA (#15400054, Gibco-ThermoFisher) and
264 frozen at 10^6 cells/vial in 10% DMSO (#D4540, Sigma-Aldrich). All cells used in our experiments
265 are mycoplasma-free.
266
267 **Scratch assay**
268 For scratch assay, SCC25 cells were grown to confluence. A central scratch of 1mm of distance
269 was produced using a silicon scraper. Medium was changed immediately with conditioned
270 medium: Control group medium contained the anti-mitotic Aphidicolin (1ug/ml; # A4487 Sigma-
271 Aldrich) and DMSO (#D8418; Sigma-Aldrich); Treated group contained Aphidicolin (1ug/ml; #
272 A4487 Sigma-Aldrich) and CB103 (100µM; # HY-135145 MedChemExpress). Fresh conditioned
273 medium was used for medium changes every two days for 10 days. Images were taken at 20X
274 every day at the same time of the day using a Leica DMIL LED inverted microscope mounting a
275 Leica camera DFC295. Four wells per conditions were analyzed. Quantification of cell-free areas
276 was performed using FIJI/ImageJ free software.
277
278 **Cell immunofluorescence**
279 Treated SCC25 cells were plated on hatched coverslips at 20.000cells/well. Cells were fixed with
280 PFA4% for 15min at 4°C. After PBS washing, cells were permeabilized 30 min in 0.1% triton and
281 then blocked using a solution of 10% FBS, 0,1% triton in PBS. Primary antibodies were diluted in
282 blocking buffer and incubated overnight. Primary antibodies a-Vinculin 1:500 (#90227 Millipore)

283 was used for immunofluorescence on cells and detected via secondary antibody donkey anti-mouse
284 IgG 546, Alexa Fluor 546 (dilution 1:1000; Invitrogen). Nuclear counterstaining was performed
285 using DAPI (4',6-Diamidino-2-Phenylindole, Dihydrochloride, #D1306, Invitrogen).
286 TRITC-conjugated Phalloidin staining of actin filaments was performed as indicated by the
287 manufacturer (1:1000 for 1h incubation at room temperature; Millipore # 90228). Mounting in
288 Mowiol 4-88/Glycerol (#81381 and #G-6279, Sigma-Aldrich).
289
290 **Time-lapse imaging**
291 Low passage SCC25 cells were treated with CB103 (100µM; # HY-135145 MedChemExpress) or
292 DMSO (#D8418; Sigma-Aldrich) for 4 days and then plated at 10000 cells/well in an 8-wells µ-
293 Slide high glass bottom (#80807, Ibidi). Cells were observed under an Olympus ScanR HCS at
294 20X with controlled environmental conditions (CO2 5% and 37°C) for 3h, taking an image every
295 3 minutes. For analysis, Imaris 9.9 (Bitplane) spot and tracking function was used to automatically
296 quantify the displacement length.
297
298

299 **Results**

300

301 **Physiological Distribution and Localization of Notch1, Dll4, and Jag1 in the Tongue**
302 **Epithelium**

303 To investigate how the Notch signalling pathway is activated in OSCC, we initially sought to
304 examine receptor-ligand interactions in the keratinized epithelium of the tongue, the primary site
305 of OSCC development. Since different receptor-ligand combinations can either activate or inhibit
306 Notch signaling, identifying the specific interactions present in normal tissue is a critical first step
307 in understanding how the pathway is regulated in the oral mucosa.

308 To map Notch1 receptor activity in vivo, we used an inducible transgenic reporter mouse model,
309 *Notch1*^{CreERT}*:R26mTmG*$^{fl/fl}$, which allows for mGFP labeling of Notch1-expressing cells following
310 tamoxifen administration (Figure 1A). This system enabled us to monitor Notch1 activation over
311 time and to track the behavior and contribution of labeled cells as the tissue transitions from a
312 healthy state to advanced stages of OSCC.

313 Using light-sheet microscopy (mesoSPIM), we generated a 3D reconstruction of the entire tongue
314 epithelium and observed Notch1-driven mGFP expression in both ventral and dorsal regions
315 (Figure 1B, Movie 1). Cross-sections of adult tongues provided more detailed views of Notch1
316 localization within the stratified epithelium, confirming its broad distribution across both surfaces
317 (Figure 1C). In *Notch1*^{CreERT}*:R26mTmG*$^{fl/fl}$ mice, Notch1:mGFP-positive cells were restricted to
318 the multilayered tongue epithelium, while unrecombined regions retained expression of the
319 mTomato cassette (Figure 1D). Both endogenous Notch1 protein and Notch1-driven mGFP were
320 detected from the basal layer up to the stratum granulosum (Figures 1C, 1D).

321 We then examine the spatial distribution of Notch-ligands Jagged1 (Jag1) and Delta-like-4 (Dll4)
322 in the tongue epithelium. We identified a compartmentalized expression pattern with mutually
323 exclusive localization (Figures 1E and 1F). Jag1 was present on both the dorsal and ventral sides
324 of the tongue, with staining in the spaces between filiform papillae of the dorsal region (Figure
325 1E). In contrast, Dll4 was exclusively localized in the epithelium of the dorsal tongue, specifically
326 on the outer surface of the filiform papillae (Figure 1F). This complementary expression pattern
327 of the two ligands suggests a potentially distinct role for Notch1-Jagged1 versus Notch1-Dll4
328 interactions in the physiology of tongue keratinocytes.
329

330 **Mutually exclusive distribution patterns of Dll4 and Jag1 in the tongue epithelium of OSCC**

331 To model the progressive stages of tongue squamous cell carcinoma, we administered the
332 carcinogenic substance 4-Nitroquinoline N-oxide (4NQO) in the drinking water of 6-weeks-old
333 mice for a duration of 16 weeks (Supplementary Figure 1A) [45]. As previously reported, chronic
334 exposure to 4NQO for 16 weeks induces hyperplasia and dysplasia in the tongue epithelium [46].
335 After an additional 10-week washout period, the tissue progresses to carcinoma with 100%
336 penetrance. Histological analysis of 22-week-old mice revealed epithelial hyperplasia,
337 leukoplakia, and hyperkeratinization, primarily on the dorsal side of the tongue and occasionally
338 on the ventral side (Supplementary Figures 1A, 1B, 1C). By 32 weeks of age, histological evidence
339 of carcinoma in situ was observed on the dorsal epithelium of the tongue (Supplementary Figures
340 1B, 1C) [46]

341 To study the role of Notch in OSCC initiation, we firstly treated *Notch1*^{CreERT}*:R26mTmG*$^{fl/fl}$ mice
342 with 4NQO or DMSO and analyzed the tissue at 22 weeks of age (Figures 2A). In 4NQO-treated
343 mice, we observed specific Notch-driven mGFP expression localized to the hyperplastic

344 epithelium (Figure 2B), indicating active Notch signaling within the cell population driving
345 malignant transformation. Next, we assessed the distribution of the Notch ligands Dll4 and Jag1
346 at this early stage. Dll4 staining was restricted to the hyperplastic epithelium (Figure 2C), while
347 Jag1 immunolabelling was notably absent in this same region (Figure 2D, white arrows and dashed
348 area). Interestingly, Jag1 expression displayed a gradual decline: it remained at physiological
349 levels in unaffected tongue regions distant from the epithelial overgrowth (Figure 2D, red arrows),
350 decreased progressively in the tissue bordering the hyperplastic area (Figure 2D, yellow arrows),
351 and became undetectable within the tumor's central core (Figure 2D, white arrows).
352 To determine whether the exophytic growth exhibited undifferentiated characteristics at this early
353 stage of the disease, we performed labeling for the undifferentiated markers Sox2 and K5,
354 alongside the mature keratinocyte marker K10 [47,48]. Sox2 and K5 were highly expressed in the
355 exophytic mass, whereas K10 was absent, indicating that the growing mass predominantly consists
356 of undifferentiated progenitor cells (Figure 2E).

357 We next aimed to determine whether the Notch1-Dll4 signaling axis remains active throughout
358 OSCC progression or is restricted to the tumor initiation phase. To address this, we analyzed
359 4NQO-treated *Notch1CreERT:R26mTmGfl/fl* mice at a later time point (32-weeks-old; Figure
360 3A). While DMSO-treated mice showed a similar pattern to the one observed in 22-weeks-old
361 tissue (Figure 3B, upper panel), carcinoma in situ lesions exhibited widespread Notch1-driven
362 mGFP labeling (Figure 3B, lower panel). Consistent with our previous observations, Jag1
363 expression was largely absent from the tumor mass but persisted in the adjacent tissue (Figures
364 3C), whereas strong Dll4 staining was detected within the exophytic tumor growth (Figure 3D).
365 Thus, the Notch1-Dll4 interaction appears to be a constant throughout the course of OSCC
366 development, from initiation to advanced lesions.

367 **Notch1-Dll4 signature correlate with maintenance of undifferentiation and early epithelial**
368 **to mesenchymal transition.**

369 As the Notch signaling have been implicated in the maintenance of stem cell identity in a variety
370 of tissues[49], we explored whether the presence of Notch1-Dll4 signaling correlates with
371 undifferentiation in OSCC lesions. To this end, 32-week-old mice tissue was stained for the
372 progenitor markers Sox2 and K5. In 4NQO-treated mice, these markers label the majority of
373 malignant cells, while in DMSO-treated controls, Sox2 and K5 staining was restricted to the basal
374 epithelial layer of the tongue (Supplementary Figures 2A and 2B) [50,51]. Conversely, the
375 differentiation marker K10 was confined in the cornified layer of the healthy tongue epithelium
376 (Supplementary Figure 2C), while remaining undetectable in the 4NQO-induced exophytic
377 growth. Finally, malignant epithelial cells retain the expression of the pan-epithelial marker E-
378 Cadherin (E-Cad)[52] (Supplementary Figure 2D). Taken together, these results suggest impaired
379 differentiation and an expansion of progenitor-like cells within the 4NQO-induced tumor
380 (Supplementary Figure 2C).
381 Next, we investigated whether inhibiting Notch in tongue keratinocytes directly affects stem cell
382 behavior [67]. To assess this, we performed an organoid formation assay using epithelial stem cells
383 isolated from the tongue. In control cultures treated with DMSO, organoids consistently formed
384 within 5 days, with an average diameter of 122.43 μm ± 36.9. However, in cultures treated with
385 the Notch inhibitor CB103, organoid formation was completely disrupted: Cells remained as single
386 cells or small clusters, with an average diameter of 20.21 μm ± 7.19 (DMSO vs. CB103,
387 $p \leq 0.0001$). These results suggest that Notch signaling is essential for maintaining the stem cell
388 functions required for organoids initiation and growth (Figure 4A).

389 To gain insight into the molecular changes driving malignant transformation, we performed further
390 analyses at the 32-weeks-old stage. After separating the tongue's outer epithelium from the
391 underlying connective tissue [42] total RNA was extracted for downstream analyses (Figure 4B).
392 qRT-PCR on 4NQO-treated epithelium showed an important increase in *Dll4* expression compared
393 to DMSO-treated epithelium (Figure 4C). Interestingly, the *Hes*-family of target genes remained
394 largely unaffected, whereas *Hey1* and *Hey2* (Hairy and enhancer of split-related with YPRW motif
395 protein) were significantly reduced in 4NQO-treated epithelia (Figure 4C). To obtain a
396 comprehensive view of the transcriptional changes, we additionally performed bulk RNA
397 sequencing analyses. Gene Set Enrichment Analysis (GSEA) revealed a significant enrichment of
398 the Notch signaling signature (Figure 4D), which was further supported by the volcano plot
399 highlighting a pronounced upregulation of *Dll4* in 4NQO-treated samples (Figure 4F). We
400 identified 3331 differentially expressed genes in 4NQO-treated versus DMSO-treated epithelia (p-
401 value threshold $p \leq 0.01$; Supplementary Method 1). The heatmap shows changes in genes mainly
402 involved in cell differentiation processes (Cluster 2 and Cluster 3), molecular pathways regulating
403 cell fate determination (Cluster 1 and Cluster 5), extracellular matrix rearrangement (Clusters
404 1,2,3,4), and cell motility (Cluster 3) (Figure 4E, Supplementary Table 3). Additional GSEA
405 showed changes in keratinocyte differentiation and cornification (Figure 4G and Supplementary
406 Figure 3). These results align with our phenotyping data, which show that the Notch1-Dll4 axis is
407 associated with the maintenance of an undifferentiated state.
408 We then conducted interactome analyses to examine changes in the tongue's epithelia upon 4NQO
409 and DMSO treatments. Independent *Enrichr (https://maayanlab.cloud/Enrichr/)* analyses
410 identified alteration of *Runt-related transcription factor 1 (Runx1)* amongst others (e.g., *p21, p300*
411 and *Stat3*) (Supplementary Figure 4). Importantly, this alteration is specific to *Runx1*, as other

412 members of the *Runx* family were not significantly altered (Supplementary Figure 4B). As *Runx1*
413 has been previously linked to Notch pathway activation[53–55], we wanted to demonstrate the
414 distribution of the Runx1 protein in the tumorigenic epithelium of the tongue. Indeed, a strong
415 Runx1 staining was detected in the tumor mass of the 4NQO-treated mice (Supplementary Figure
416 5A), while the Runx1 labelling was confined to the stratum basale and stratum spinosum of the
417 DMSO-treated mice. Furthermore, strong immunostaining against p63, a marker of
418 undifferentiated keratinocytes[56], was detected in the tumor mass of 4NQO-treated mice
419 (Supplementary Figure 5B) [53,57–62] . Together, these findings suggest that Notch1-Dll4 signaling
420 is closely linked to the expansion of progenitor-like cell populations in OSCC lesions, supporting
421 its role in maintaining an undifferentiated state during malignant transformation.
422
423 At more advanced stages of OSCC progression, malignant cells residing within the exophytic mass
424 may become invasive by undergoing epithelial-to-mesenchymal transition (EMT) [63]. Using light-
425 sheet microscopy (SPIM), we analyzed 4NQO-treated mice to identify the time window when
426 basal lamina dissolution begins. In 22-week-old mice, digital sectioning revealed an uninterrupted
427 basal lamina underneath the epithelial overgrowth (Supplementary Figure 6A, yellow arrows;
428 Movie 2). In 32-week-old mice, we observed a localized area of basal lamina degradation, allowing
429 the malignant overgrowth to directly interface with the underlying mesenchyme (Supplementary
430 Figure 3B, white arrows; Movie 3).
431 To investigate the molecular changes that may contribute to the dissolution of the basal lamina
432 observed in SPIM imaging, we examined our sequencing data. We identified an EMT signature
433 through GSEA, along with changes in anchoring junctions (Figure 4H). Gene Ontology analysis
434 for biological processes and cellular components further confirmed alterations in cell-cell and cell-

435 to-ECM communication, as well as cell migration (Figure 4I). To validate EMT onset at this stage,
436 we assessed the expression of the mesenchymal marker Vimentin (*VIM*), components of the
437 extracellular matrix Tenascin (*TNC*), and members of the zinc-finger transcription factor family
438 *Snail*. Transcriptomic analyses confirmed their upregulation, together with the early EMT markers
439 ZEB1, ZEB2 (Figure 4L and 4M).
440 While technical limitations of the 4NQO model prevent us from capturing the full extent of the
441 EMT process and metastasis formation, our data indicate that EMT initiation occurs at the 32-
442 week-old stage following 4NQO exposure, with changes in tissue architecture, molecular
443 signatures, and the upregulation of key markers of cellular transformation.
444
445 **Invasive squamous cells conserve their dependency from the Notch1-Dll4 signaling axis**
446 To confirm the progression toward an invasive phenotype, we analyzed a more advanced stage of
447 our OSCC model at 38-weeks-old. Tongue sections from *R26:mTomato* mice were stained with
448 the epithelial markers K14 and P63. This labeling revealed clusters of epithelial cells embedded
449 within the stromal tissue of the tongue (Figures 5B and 5C). These findings led us to hypothesize
450 that carcinoma in situ cells had breached the basal lamina and begun invading the underlying
451 connective tissue. As confirmation that EMT was occurring at this stage, we examined the
452 expression patterns of Snai1 and the adhesion molecule regulator E-cadherin [64,65]. Snail-positive
453 staining was detected in cells within the invasive tumor mass of 4NQO-treated mice (Figure 5D,
454 white arrows), whereas such labeling was absent in DMSO-treated controls. We then assessed the
455 distribution of Vimentin and E-cadherin, markers of mesenchymal and epithelial identity,
456 respectively [65,66]. A subset of cells within the tumor mass coexpressed vimentin and E-cadherin
457 (Figure 5E, yellow arrows), thus confirming an ongoing EMT process.

458 We therefore sought to clarify if the Notch1-Dll4 signaling axis is also involved in the process of
459 tumor invasion observed in 38-weeks-old mice. *Notch1*^{CreERT}*:R26mTmG*$^{fl/fl}$ mice were used to trace
460 Notch1-expressing cells and their progeny (Figure 6A). In DMSO-treated mice, *mGFP* expression
461 remained restricted to the epithelial layers (Figure 6B). Conversely, in 4NQO-treated mice, mGFP-
462 labeled cells were observed within the carcinoma mass invading the mesenchyme (Figure 6C). We
463 next performed immunolabeling for the Notch1 protein. A widespread Notch1 signal labeled the
464 infiltrating mass of 4NQO-treated mice, while in DMSO-treated mice Notch1 expression remained
465 confined to the healthy tongue epithelium (Figure 6D). Finally, we examined the expression of
466 Dll4 in the invasive aberrant epithelium using *R26:mTomato* mice. Analysis of DMSO-treated
467 mice confirmed the expression of Dll4 in the dorsal portion of the filiform papillae, as previously
468 observed (Figure 6E and 1F). In 4NQO-treated mice, labeling for Dll4 was broadly present in the
469 infiltrating mass (Figure 6E). Our findings suggest a conserved paradigm governing tumor
470 progression, where the Notch1-Dll4 axis remains central throughout the phases of hyperplastic
471 growth, carcinoma in situ and the most advanced, invasive stages of the disease.
472

473 **The Notch signaling pathway regulates malignancy in human OSCC**

474 To evaluate the clinical relevance of the Notch pathway in OSCC, we examined the expression of
475 JAG1 and DLL4 in human tissue samples. We first performed Hematoxylin and Eosin (H&E)
476 staining on tissues from HPV-negative adult patients with primary tumors. This allowed us to
477 identify characteristic SCC features, including dysplastic epithelium, mitotic figures, and
478 abnormal keratin accumulation (Figure 7, overview). Based on these histological criteria, we
479 distinguished healthy tissue (Figure 7A) from hyperplastic (Figure 7D) and carcinoma samples
480 (Figure 7G).

481 Jag1 and Dll4 expression were then compared across these different tissue types. DLL4 showed
482 diffuse expression in the healthy epithelium (Figure 7B), with increased levels observed in
483 hyperplastic tissue (Figure 7E) and consistently high expression in carcinoma nests (Figure 7H).
484 In contrast, JAG1 staining in healthy tissue was limited to small, localized pockets, and its
485 expression varied across different regions of the carcinoma samples (Figure 7C and Figure 7F,7I).

486 To further investigate the molecular regulation of the Notch pathway in the human context, we
487 treated hSCC25 cell line (#CRL-1628, ATCC/LGC) with CB103, a pan-blocker of the Notch-
488 transcriptional activation complex[67] (Figure 8A). Interestingly, quantitative RT-PCR revealed a
489 specific downregulation of the *DLL4* expression, while *JAG1* levels remain largely unchanged
490 (Figure 8B). Additionally, CB103 treatment resulted in decreased expression of *SOX2* and *P63*
491 (Figure 8B), suggesting a direct link between Notch activity and the maintenance of an
492 undifferentiated state.
493 To further investigate the molecular impact of CB103 treatment, we performed bulk seqRNA
494 comparing DMSO- versus CB103-treated hSCC25 cells. This analysis identified 3329
495 differentially expressed genes ($p \leq 0.01$; Supplementary Method 2), with the top 2000 genes
496 visualized in a hierarchical clustering heatmap (Figure 8D). The heatmap highlights alterations in
497 genes involved in epithelial differentiation (Cluster 3, 4 and Cluster 5), cell-to-cell adhesion
498 (Cluster 3), cytoskeleton organization (Cluster 4, Cluster 5) and chemotaxis (Cluster 1) (Figure
499 8D, Supplementary Table 4). GO analysis for cellular components and biological processes, along
500 with *Enrichr* analyses, further supported these findings by identifying alterations in intermediate
501 filaments, cell-to-cell adhesion, and cell-to-ECM interactions (Figure 8C, Supplementary Figure
502 7A and Supplementary Figure 7B). Paralleling our findings in the mouse model, GSEA analysis
503 revealed significant changes in keratinization processes and keratinocytes differentiation (Figure

504 8E). Additionally, MA and volcano plot analysis indicated an upregulation in the expression of
505 keratins (Figure 8F), as well as a change in the expression of integrins and ECM molecules
506 (Supplementary Figure 7C). Together with GSEA results (Figure 8G-I), these data suggest that
507 CB103-treated cells undergo structural modifications and remodeling of anchoring molecules.
508 We hypothesized that such changes could affect cell motility, a crucial factor in acquiring an
509 invasive phenotype during cancer progression. We therefore aimed to explore the functional
510 consequences of CB103 treatment. Among the differentially expressed signatures, we identified
511 enrichment in genes associated with desmosomal complexes and apical junctions (Figures 9A, 9B
512 and 9D). qRT-PCR validation confirmed a significant upregulation of desmosome-associated
513 proteins upon CB103 treatment, including desmoplakin, desmoglein, and desmocollin (Figure 9C).
514 Consistently, CB103-treated cells exhibited a marked increase in the number of adhesive
515 complexes compared to DMSO-treated controls (Figures 9E and 9F)[68,69], reinforcing the role of
516 Notch inhibition in enhancing cell–cell adhesion. Finally, we conducted scratch assays and
517 monitored the progression of migrating cells over a period of 10 days (Figures 9G and 9H).
518 DMSO-treated cells were able to fully reform the monolayer within a ten-day timeframe, in
519 contrast to CB103-treated cells, which were unable to recolonize the cell-free zone (Figure 9G).
520 To further confirm the reduced motility of CB103-treated cells, we performed time-lapse analysis.
521 CB103-treated cells exhibited significantly reduced motility when compared to cells treated with
522 DMSO (Figures 9I and 9J; Movies 4 and 5). These results indicate that selective Notch inhibition
523 by CB103 markedly alters the expression of structural components within adhesive complexes that
524 anchor epithelial cells to the extracellular matrix, ultimately reducing the migration of human
525 carcinoma cells.
526

527 Overall, our findings from both murine and human models highlight the critical role of the Notch1-
528 Dll4 axis in maintaining undifferentiation and promoting motility. Disrupting this pathway
529 effectively impairs key drivers of OSCC malignancy.
530
531 **Discussion**
532
533 The Notch signaling pathway is a central regulator of carcinogenic transformation in a variety of
534 epithelial tumors, including lung, cervical, colon, and pancreatic cancers [70–73]. The dysregulation
535 of Notch is context-dependent and can shift from an activator to an inhibitor, depending on the
536 organ and the type of tissue affected [74–76]. Currently, a debate exists on whether the Notch pathway
537 acts as an oncogene or tumor suppressor in OSCC, and its exact role in this type of cancer remains
538 largely unknown [19,77,78]. Since Notch activity is strongly influenced by the specific receptor-ligand
539 interactions within a tissue, our first goal was to identify how these combinations evolve across
540 healthy tissue, initiation, and advanced stages of OSCC. To achieve this, we used the
541 *Notch1CreERT:R26mTmGfl/fl* transgenic line and studied Notch1-expressing cells and their
542 progeny throughout the progressive stages of malignant transformation. Short tamoxifen pulses
543 allowed precise control of the reporter activation, providing information on which cells had active
544 Notch1 at specific time points. Pulse-and-chase experiments instead, tracked labelled cells over
545 extended periods, revealing their movements and dynamic behavior as the cancer progresses and
546 its structure evolves. Through detailed phenotypic characterization, our findings suggest that
547 Notch signaling contributes to OSCC development and progression by preferentially interacting
548 with the Dll4 ligand rather than Jag1. Gene expression analyses confirmed that *Dll4* is the most
549 significant gene of the Notch pathway to be differentially regulated in OSCC condition. The
550 preferential binding of Notch1 to Dll4 in the tumorigenic epithelium ultimately leads to the

551 downregulation of *Hey1* and *Hey2*, while the expression of other Notch-specific target genes, such
552 as *Hes1* and *Hes2,* remains largely unaffected. The mutually exclusive expression of the Jag1 and
553 Dll4 ligands regulates fate definition and undifferentiation in a variety of tissues (e.g., during
554 angiogenesis and hematopoiesis)[40,79,80]. Similarly in our system, the selection between the Notch1-
555 Dll4 versus Notch1-Jag1 interaction observed in OSCC coincides with sustained keratinocyte
556 undifferentiation. The Notch1/Dll4-expressing keratinocyte progenitors retain their immature
557 state, resulting in the expansion of the undifferentiated portion of the tongue epithelium.
558 Important downstream changes occur during Notch pathway dysregulation in OSCC. Our
559 transcriptomic analyses reveal a complex scenario of crosstalk between pathways sustaining oral
560 carcinoma. Interestingly, p63 and Runx1 cooperate with the Notch pathway, similarly to what has
561 been found in other tissues. In skin keratinocytes a bidirectional crosstalk between Notch and p63
562 suggest a complex regulation of differentiation occurring at various levels (from regulation of
563 transcription to indirect regulation of the Notch pathway). A high expression of P63 correlates
564 with poor prognosis in patients with OSCC of the tongue[53,54,64,81–8375]. Our model showed a similar
565 correlation, with an undifferentiated mass coherently expressing P63 and Notch1-Dll4. In HNSCC
566 screenings, the transcription factor RUNX1 was found to be significantly increased and thus, has
567 been suggested as a prognostic marker [83,84]. RUNX1 upregulation drives tumor progression and
568 metastasis, while suppression of RUNX1 inhibits HNSCC cell proliferation and migration [84,84,85].
569 In other settings, such as mammalian hematopoiesis, Runx1 controls the expansion, specification
570 and self-renewal of stem cells in a Notch-dependent manner [86 87,88]. We have found a similar
571 scenario in our system, where both transcriptomic approaches and immunostainings show a
572 widespread expression of Runx1 and Notch1-Dll4 with an analogous expression pattern.

573 Continuous epithelial growth gives rise to a malignant mass with the potential of invading the
574 underling stroma[11]. In the invasive growth, we identified typical features of EMT, such as basal
575 lamina dissolution, overexpression of ZEB1, ZEB2 and Snail1 and cells co-expressing Vimentin
576 and E-cadherin. Transcriptomic analysis confirmed a specific hallmark signature for EMT in the
577 epithelium of 4NQO-treated mice. Importantly, cells of epithelial origin growing within the
578 mesenchyme maintain the expression of Dll4. Consequently, we identified the Notch-Dll4 axis
579 throughout all phases of OSCC progression, spanning from the initial hyperplastic phase to the
580 most advanced invasive stages, highlighting its promising potential as a diagnostic tool.
581 To strengthen the translational impact of our findings, we analyzed human malignant tissue and
582 confirmed elevated expression of DLL4. Dll4 blockers have been proposed for the treatment of
583 other epithelial tumors (e.g., intestinal tumors) primarily aiming to limit angiogenesis [89]. Since
584 OSCC growth is not strictly dependent on vascularization, a locally administered blocker could
585 directly target malignant epithelial cells in this tumor. Immunotherapy specifically targeting Dll4
586 combined to chemotherapy has been applied to treat solid tumors (e.g., pancreatic and lung
587 cancers) [90–93], with positive results spanning from a reduction of tumor growth to a decrease in the
588 reoccurrence rate [94–96]. Given the redundancy of the Notch pathway and the frequent activation of
589 compensatory mechanisms when a single component is targeted, we hereby adopted a broader
590 strategy to test the therapeutic potential of pan-Notch blockers in OSCC. The Notch
591 pharmacological inhibitor CB103 is increasingly gathering attention in cancer treatments, in view
592 of its high stability and unbeaten specificity in targeting the Notch pathway [67,97,98]. Several clinical
593 trials are currently in place to determine its usage as a therapeutic agent in carcinomas (clinical
594 trials: NCT03422679, NCT04714619) as well as leukemias and lymphomas (clinical trials:
595 NCT03422679, NCT05464836). In our system, SCC25 cells treated with CB103 displayed a

596 significant reduction in *DLL4* expression, with no observable change in *JAG1* expression,
597 confirming the crucial role of the NOTCH-DLL4 signaling axis in OSCC. Importantly, the
598 expression of undifferentiation markers SOX2 and P63 is significantly reduced in CB103-treated
599 cells, while transcriptomic analysis reveals induction of keratinization. These *in vitro* results
600 validate the *in vivo* findings in mice and denote the connection between an active NOTCH-Dll4
601 signaling axis and the prolonged undifferentiation cell state within OSCC. We finally tested the
602 functional effects of Notch blockage in OSCC cell behavior. We recorded a dramatic reduction in
603 cell migration when SCC25 cells were treated with CB103. This is accompanied by an increase in
604 adhesive complexes (focal adhesions and desmosomes), suggesting that NOTCH regulates cell
605 movement and is essential for the acquisition of tumor's invasive properties.
606 In conclusion, the present findings show that the Notch1-Dll4 signaling axis plays a crucial role in
607 the initiation and development of OSCC, contributing to the acquisition of critical oncogenic
608 features.
609
610

611 **Acknowledgements**

612 This work was supported by the University of Zurich, the Krebsliga (KFS-4890-08-2019-R)
613 (T.A.M.), the Julius Klaus-Stiftung (C.P.), Stiftung Julius Müller zur Unterstützung der
614 Krebsforschung (C.P.) and the Olga Mayenfisch Stiftung (C.P.). We thank Prof. Spyros Artavanis-
615 Tsakonas (Harvard Medical School, Harvard University) for providing *Notch1*^{creER} mice.

616 Imaging was performed with equipment maintained by the Center for Microscopy and Image
617 Analysis, University of Zurich. The authors gratefully acknowledge the Functional Genomics
618 Center Zurich (FGCZ) of University of Zurich and ETH Zurich for the support on analyses.

619

620

621 **References**

622

623 1. Ferlay, J. *et al.* Estimating the global cancer incidence and mortality in 2018: GLOBOCAN
624 sources and methods. *Int J Cancer* **144**, 1941–1953 (2019).
625 2. Bray, F. *et al.* Global cancer statistics 2018: GLOBOCAN estimates of incidence and
626 mortality worldwide for 36 cancers in 185 countries. *CA: A Cancer Journal for Clinicians*
627 **68**, 394–424 (2018).
628 3. Johnson, D. E. *et al.* Head and neck squamous cell carcinoma. *Nat Rev Dis Primers* **6**, 92
629 (2020).
630 4. Cramer, J. D., Burtness, B., Le, Q. T. & Ferris, R. L. The changing therapeutic landscape of
631 head and neck cancer. *Nat Rev Clin Oncol* **16**, 669–683 (2019).
632 5. Duprez, F. *et al.* Distant metastases in head and neck cancer: Distant metastases in head and
633 neck cancer. *Head & Neck* **39**, 1733–1743 (2017).
634 6. Pisani, P. *et al.* Metastatic disease in head & neck oncology. *Acta Otorhinolaryngol Ital* **40**,
635 S1–S86 (2020).
636 7. Eckert, R. L. & Rorke, E. A. Molecular biology of keratinocyte differentiation. *Environ*
637 *Health Perspect* **80**, 109–116 (1989).
638 8. Franchi, A. & Skalova, A. Undifferentiated and dedifferentiated head and neck carcinomas.
639 *Semin Diagn Pathol* **38**, 127–136 (2021).
640 9. Zhou, H.-M., Zhang, J.-G., Zhang, X. & Li, Q. Targeting cancer stem cells for reversing
641 therapy resistance: mechanism, signaling, and prospective agents. *Signal Transduct Target*
642 *Ther* **6**, 62 (2021).

643 10. Müller, S. Update from the 4th Edition of the World Health Organization of Head and Neck
644 Tumours: Tumours of the Oral Cavity and Mobile Tongue. *Head Neck Pathol* **11**, 33–40
645 (2017).
646 11. Pai, S. I. & Westra, W. H. Molecular pathology of head and neck cancer: implications for
647 diagnosis, prognosis, and treatment. *Annu Rev Pathol* **4**, 49–70 (2009).
648 12. Byers, R. M. *et al.* Frequency and therapeutic implications of 'skip metastases' in the neck
649 from squamous carcinoma of the oral tongue. *Head Neck* **19**, 14–19 (1997).
650 13. Kuperman, D. I. *et al.* Squamous cell cancer of the head and neck with distant metastasis at
651 presentation. *Head Neck* **33**, 714–718 (2011).
652 14. Califano, J. *et al.* Genetic progression and clonal relationship of recurrent premalignant head
653 and neck lesions. *Clin Cancer Res* **6**, 347–352 (2000).
654 15. Puram, S. V. *et al.* Cellular states are coupled to genomic and viral heterogeneity in HPV-
655 related oropharyngeal carcinoma. *Nat Genet* **55**, 640–650 (2023).
656 16. Bai, Y. *et al.* YBX1 integration of oncogenic PI3K/mTOR signalling regulates the fitness of
657 malignant epithelial cells. *Nat Commun* **14**, 1591 (2023).
658 17. Stransky, N. *et al.* The Mutational Landscape of Head and Neck Squamous Cell Carcinoma.
659 *Science* **333**, 1157–1160 (2011).
660 18. Sequeira, I. *et al.* Genomic landscape and clonal architecture of mouse oral squamous cell
661 carcinomas dictate tumour ecology. *Nat Commun* **11**, 5671 (2020).
662 19. Agrawal, N. *et al.* Exome sequencing of head and neck squamous cell carcinoma reveals
663 inactivating mutations in NOTCH1. *Science* **333**, 1154–1157 (2011).

664 20. Fan, W.-L. *et al.* Prognostic Genetic Biomarkers Based on Oncogenic Signaling Pathways
665 for Outcome Prediction in Patients with Oral Cavity Squamous Cell Carcinoma. *Cancers*
666 *(Basel)* **13**, 2709 (2021).
667 21. Loganathan, S. K. *et al.* Rare driver mutations in head and neck squamous cell carcinomas
668 converge on NOTCH signaling. *Science* **367**, 1264–1269 (2020).
669 22. Artavanis-Tsakonas, S. Notch Signaling: Cell Fate Control and Signal Integration in
670 Development. *Science* **284**, 770–776 (1999).
671 23. Casey, L. M. *et al.* Jag2-Notch1 signaling regulates oral epithelial differentiation and palate
672 development. *Dev. Dyn.* **235**, 1830–1844 (2006).
673 24. Mustonen, T. *et al.* Lunatic fringe, FGF, and BMP regulate the Notch pathway during
674 epithelial morphogenesis of teeth. *Dev Biol* **248**, 281–293 (2002).
675 25. Mitsiadis, T. A., Henrique, D., Thesleff, I. & Lendahl, U. Mouse Serrate-1 (Jagged-1):
676 expression in the developing tooth is regulated by epithelial-mesenchymal interactions and
677 fibroblast growth factor-4. *Development* **124**, 1473–1483 (1997).
678 26. Mitsiadis, T. A., Lardelli, M., Lendahl, U. & Thesleff, I. Expression of Notch 1, 2 and 3 is
679 regulated by epithelial-mesenchymal interactions and retinoic acid in the developing mouse
680 tooth and associated with determination of ameloblast cell fate. *Journal of Cell Biology* **130**,
681 407–418 (1995).
682 27. Porcheri, C. & Mitsiadis, T. A. Notch in Head and Neck Cancer. *Adv Exp Med Biol* **1287**,
683 81–103 (2021).
684 28. Artavanis-Tsakonas, S., Rand, M. D. & Lake, R. J. Notch signaling: cell fate control and
685 signal integration in development. *Science* **284**, 770–776 (1999).

686 29. Kopan, R. & Ilagan, M. X. G. The canonical Notch signaling pathway: unfolding the
687 activation mechanism. *Cell* **137**, 216–233 (2009).
688 30. Gordon, W. R., Arnett, K. L. & Blacklow, S. C. The molecular logic of Notch signaling--a
689 structural and biochemical perspective. *J Cell Sci* **121**, 3109–3119 (2008).
690 31. Siebel, C. & Lendahl, U. Notch Signaling in Development, Tissue Homeostasis, and Disease.
691 *Physiological Reviews* **97**, 1235–1294 (2017).
692 32. Louvi, A. & Artavanis-Tsakonas, S. Notch and disease: A growing field. *Seminars in Cell &*
693 *Developmental Biology* **23**, 473–480 (2012).
694 33. Yoshida, R. *et al.* The pathological significance of Notch1 in oral squamous cell carcinoma.
695 *Lab. Invest.* **93**, 1068–1081 (2013).
696 34. Setoguchi. Upregulation of Notch pathway molecules in oral squamous cell carcinoma. *Int J*
697 *Oncol* **36**, (2010).
698 35. Sakamoto, K. *et al.* Reduction of NOTCH1 expression pertains to maturation abnormalities
699 of keratinocytes in squamous neoplasms. *Laboratory Investigation* **92**, 688–702 (2012).
700 36. Sawangarun, W. *et al.* Loss of Notch1 predisposes oro-esophageal epithelium to
701 tumorigenesis. *Experimental Cell Research* **372**, 129–140 (2018).
702 37. Natsuizaka, M. *et al.* Interplay between Notch1 and Notch3 promotes EMT and tumor
703 initiation in squamous cell carcinoma. *Nat Commun* **8**, 1758 (2017).
704 38. Fre, S. *et al.* Notch lineages and activity in intestinal stem cells determined by a new set of
705 knock-in mice. *PLoS One* **6**, e25785 (2011).
706 39. Muzumdar, M. D., Tasic, B., Miyamichi, K., Li, L. & Luo, L. A global double-fluorescent
707 Cre reporter mouse. *Genesis* **45**, 593–605 (2007).

708 40. Porcheri, C. *et al.* Notch ligand Dll4 impairs cell recruitment to aortic clusters and limits
709 blood stem cell generation. *EMBO J.* **39**, e104270 (2020).
710 41. Voigt, F. F. *et al.* The mesoSPIM initiative: open-source light-sheet microscopes for imaging
711 cleared tissue. *Nat Methods* **16**, 1105–1108 (2019).
712 42. Meisel, C. T., Pagella, P., Porcheri, C. & Mitsiadis, T. A. Three-Dimensional Imaging and
713 Gene Expression Analysis Upon Enzymatic Isolation of the Tongue Epithelium. *Front*
714 *Physiol* **11**, 825 (2020).
715 43. Driehuis, E. *et al.* Oral Mucosal Organoids as a Potential Platform for Personalized Cancer
716 Therapy. *Cancer Discov* **9**, 852–871 (2019).
717 44. Yu, G. & He, Q.-Y. ReactomePA: an R/Bioconductor package for reactome pathway
718 analysis and visualization. *Mol. BioSyst.* **12**, 477–479 (2016).
719 45. Ishida, K. *et al.* Current mouse models of oral squamous cell carcinoma: Genetic and
720 chemically induced models. *Oral Oncol* **73**, 16–20 (2017).
721 46. Bouaoud, J. *et al.* The 4-NQO mouse model: An update on a well-established in vivo model
722 of oral carcinogenesis. *Methods Cell Biol* **163**, 197–229 (2021).
723 47. Sanz-Gómez, N. *et al.* Squamous differentiation requires G2/mitosis slippage to avoid
724 apoptosis. *Cell Death Differ* **27**, 2451–2467 (2020).
725 48. Sanz-Gómez, N. *et al.* Squamous differentiation requires G2/mitosis slippage to avoid
726 apoptosis. *Cell Death Differ* **27**, 2451–2467 (2020).
727 49. Bigas, A. & Porcheri, C. Notch and Stem Cells. *Adv Exp Med Biol* **1066**, 235–263 (2018).
728 50. Vasca, V. *et al.* Keratin 5 expression in squamocellular carcinoma of the head and neck.
729 *Oncol Lett* **8**, 2501–2504 (2014).

730 51. Alam, H., Sehgal, L., Kundu, S. T., Dalal, S. N. & Vaidya, M. M. Novel function of keratins
731 5 and 14 in proliferation and differentiation of stratified epithelial cells. *Mol Biol Cell* **22**,
732 4068–4078 (2011).
733 52. Huntsman, D. G. & Caldas, C. Assignment1 of the E-cadherin gene (CDH1) to chromosome
734 16q22.1 by radiation hybrid mapping. *Cytogenet Cell Genet* **83**, 82–83 (1998).
735 53. Burns, C. E., Traver, D., Mayhall, E., Shepard, J. L. & Zon, L. I. Hematopoietic stem cell
736 fate is established by the Notch-Runx pathway. *Genes Dev.* **19**, 2331–2342 (2005).
737 54. Burns, C. E. & Zon, L. I. Notch Signaling Is Necessary and Sufficient for Runx1-Dependent
738 Stem Cell Induction in the Embryonic Aorta-Gonad-Mesonephros (AGM) Region. *Blood*
739 **104**, 4161–4161 (2004).
740 55. Islam, R. *et al.* RUNX1 colludes with NOTCH1 to reprogram chromatin in T cell acute
741 lymphoblastic leukemia. *iScience* **26**, 106795 (2023).
742 56. Crum, C. P. & McKeon, F. D. p63 in epithelial survival, germ cell surveillance, and
743 neoplasia. *Annu Rev Pathol* **5**, 349–371 (2010).
744 57. Srivastava, S. S. *et al.* Keratin 5/14-mediated cell differentiation and transformation are
745 regulated by TAp63 and Notch-1 in oral squamous cell carcinoma-derived cells. *Oncol Rep*
746 **39**, 2393–2401 (2018).
747 58. Dotto, G. P. Crosstalk of Notch with p53 and p63 in cancer growth control. *Nat Rev Cancer*
748 **9**, 587–595 (2009).
749 59. Moses, M. A. *et al.* Molecular Mechanisms of p63-Mediated Squamous Cancer
750 Pathogenesis. *Int J Mol Sci* **20**, E3590 (2019).

751 60. Ortt, K., Raveh, E., Gat, U. & Sinha, S. A chromatin immunoprecipitation screen in mouse
752 keratinocytes reveals Runx1 as a direct transcriptional target of DeltaNp63. *J Cell Biochem*
753 **104**, 1204–1219 (2008).
754 61. Nakagawa, M. *et al.* AML1/Runx1 rescues Notch1-null mutation-induced deficiency of para-
755 aortic splanchnopleural hematopoiesis. *Blood* **108**, 3329–3334 (2006).
756 62. Kouwenhoven, E. N. *et al.* Transcription factor p63 bookmarks and regulates dynamic
757 enhancers during epidermal differentiation. *EMBO Rep* **16**, 863–878 (2015).
758 63. González, M. M. *et al.* Is cancer a pure growth curve or does it follow a kinetics of
759 dynamical structural transformation? *BMC Cancer* **17**, 174 (2017).
760 64. Villarejo, A., Cortés-Cabrera, A., Molina-Ortíz, P., Portillo, F. & Cano, A. Differential role
761 of Snail1 and Snail2 zinc fingers in E-cadherin repression and epithelial to mesenchymal
762 transition. *J Biol Chem* **289**, 930–941 (2014).
763 65. Thiery, J. P. Epithelial–mesenchymal transitions in tumour progression. *Nat Rev Cancer* **2**,
764 442–454 (2002).
765 66. Dongre, A. & Weinberg, R. A. New insights into the mechanisms of epithelial–mesenchymal
766 transition and implications for cancer. *Nat Rev Mol Cell Biol* **20**, 69–84 (2019).
767 67. Lehal, R. *et al.* Pharmacological disruption of the Notch transcription factor complex. *Proc*
768 *Natl Acad Sci U S A* **117**, 16292–16301 (2020).
769 68. Ilić, D. *et al.* Reduced cell motility and enhanced focal adhesion contact formation in cells
770 from FAK-deficient mice. *Nature* **377**, 539–544 (1995).
771 69. Geiger, B., Tokuyasu, K. T., Dutton, A. H. & Singer, S. J. Vinculin, an intracellular protein
772 localized at specialized sites where microfilament bundles terminate at cell membranes. *Proc*
773 *Natl Acad Sci U S A* **77**, 4127–4131 (1980).

774 70. Avila, J. L. & Kissil, J. L. Notch signaling in pancreatic cancer: oncogene or tumor
775 suppressor? *Trends Mol Med* **19**, 320–327 (2013).
776 71. Brzozowa-Zasada, M. *et al.* Notch and its oncogenic activity in human malignancies. *Eur*
777 *Surg* **49**, 199–209 (2017).
778 72. Tyagi, A., Sharma, A. K. & Damodaran, C. A Review on Notch Signaling and Colorectal
779 Cancer. *Cells* **9**, E1549 (2020).
780 73. Rodrigues, C., Joy, L. R., Sachithanandan, S. P. & Krishna, S. Notch signalling in cervical
781 cancer. *Exp Cell Res* **385**, 111682 (2019).
782 74. Dotto, G. P. Notch tumor suppressor function. *Oncogene* **27**, 5115–5123 (2008).
783 75. Yap, L. *et al.* The opposing roles of NOTCH signalling in head and neck cancer: a mini
784 review. *Oral Dis* **21**, 850–857 (2015).
785 76. Fukusumi, T. & Califano, J. A. The NOTCH Pathway in Head and Neck Squamous Cell
786 Carcinoma. *J Dent Res* **97**, 645–653 (2018).
787 77. Cancer Genome Atlas Network. Comprehensive genomic characterization of head and neck
788 squamous cell carcinomas. *Nature* **517**, 576–582 (2015).
789 78. Johnson, D. E. *et al.* Head and neck squamous cell carcinoma. *Nat Rev Dis Primers* **6**, 92
790 (2020).
791 79. Benedito, R. *et al.* The notch ligands Dll4 and Jagged1 have opposing effects on
792 angiogenesis. *Cell* **137**, 1124–1135 (2009).
793 80. Gama-Norton, L. *et al.* Notch signal strength controls cell fate in the haemogenic
794 endothelium. *Nat Commun* **6**, 8510 (2015).
795 81. Nguyen, B.-C. *et al.* Cross-regulation between Notch and p63 in keratinocyte commitment to
796 differentiation. *Genes Dev* **20**, 1028–1042 (2006).

797 82. Ichikawa, M. *et al.* A role for RUNX1 in hematopoiesis and myeloid leukemia. *Int J*
798 *Hematol* **97**, 726–734 (2013).
799 83. Gao, L. *et al.* RUNX1 and the endothelial origin of blood. *Exp Hematol* **68**, 2–9 (2018).
800 84. Feng, X. *et al.* Elevated RUNX1 is a prognostic biomarker for human head and neck
801 squamous cell carcinoma. *Exp Biol Med (Maywood)* **246**, 538–546 (2021).
802 85. Loljung, L. *et al.* High expression of p63 is correlated to poor prognosis in squamous cell
803 carcinoma of the tongue. *J Oral Pathol Med* **43**, 14–19 (2014).
804 86. Loljung, L. *et al.* High expression of p63 is correlated to poor prognosis in squamous cell
805 carcinoma of the tongue. *J Oral Pathol Med* **43**, 14–19 (2014).
806 87. Liu, K. *et al.* RUNX1 promotes MAPK signaling to increase tumor progression and
807 metastasis via OPN in head and neck cancer. *Carcinogenesis* **42**, 414–422 (2021).
808 88. Feng, X. *et al.* Elevated RUNX1 is a prognostic biomarker for human head and neck
809 squamous cell carcinoma. *Exp Biol Med (Maywood)* **246**, 538–546 (2021).
810 89. Ridgway, J. *et al.* Inhibition of Dll4 signalling inhibits tumour growth by deregulating
811 angiogenesis. *Nature* **444**, 1083–1087 (2006).
812 90. Hidalgo, M. *et al.* A phase 1b study of the anti-cancer stem cell agent demcizumab (DEM)
813 and gemcitabine (GEM) +/- nab-paclitaxel in patients with pancreatic cancer. *JCO* **34**, 341–
814 341 (2016).
815 91. McKeage, M. J. *et al.* Phase IB Trial of the Anti-Cancer Stem Cell DLL4-Binding Agent
816 Demcizumab with Pemetrexed and Carboplatin as First-Line Treatment of Metastatic Non-
817 Squamous NSCLC. *Target Oncol* **13**, 89–98 (2018).
818 92. Coleman, M. L. *et al.* Asparaginyl hydroxylation of the Notch ankyrin repeat domain by
819 factor inhibiting hypoxia-inducible factor. *J Biol Chem* **282**, 24027–24038 (2007).

820 93. Johnson, M. *et al.* Abstract A081: A phase 1b, open-label, dose escalation and expansion
821 study of demcizumab plus pembrolizumab in patients with locally advanced or metastatic
822 solid tumors. in *Clinical Trials* A081–A081 (American Association for Cancer Research,
823 2018). doi:10.1158/1535-7163.TARG-17-A081.
824 94. Fischer, M. *et al.* Anti-DLL4 inhibits growth and reduces tumor-initiating cell frequency in
825 colorectal tumors with oncogenic KRAS mutations. *Cancer Res.* **71**, 1520–1525 (2011).
826 95. Yen, W.-C. *et al.* Anti-DLL4 Has Broad Spectrum Activity in Pancreatic Cancer Dependent
827 on Targeting DLL4-Notch Signaling in Both Tumor and Vasculature Cells. *Clin Cancer Res*
828 **18**, 5374–5386 (2012).
829 96. Smith, D. C. *et al.* A Phase I Dose Escalation and Expansion Study of the Anticancer Stem
830 Cell Agent Demcizumab (Anti-DLL4) in Patients with Previously Treated Solid Tumors.
831 *Clinical Cancer Research* **20**, 6295–6303 (2014).
832 97. Fabbro, D., Bauer, M., Murone, M. & Lehal, R. Notch Inhibition in Cancer: Challenges and
833 Opportunities. *Chimia (Aarau)* **74**, 779–783 (2020).
834 98. Perez Garcia, J. M. *et al.* First-in-human phase 1-2A study of CB-103, an oral Protein-
835 Protein Interaction Inhibitor targeting pan-NOTCH signalling in advanced solid tumors and
836 blood malignancies. *JCO* **36**, TPS2619–TPS2619 (2018).
837
838
839
840

841 **Figures legends**

842

843 **Figure 1: Notch1, Dll4 and Jag1 expression in the epithelium of the mouse tongue.**

844 A) Schematic representation illustrating the murine tongue of a *Notch1*^{CreERT}*:R26mTmG*$^{fl/fl}$ mouse
845 after tamoxifen induction and subsequent *mGFP* expression. B) MesoSPIM imaging and related
846 three-dimensional reconstruction of a whole-mount *Notch1*^{CreERT}*:R26mTmG*$^{fl/fl}$ mouse tongue.
847 Notch1-driven *mGFP* expression (green) in the raw reconstruction (left panels) and relative
848 surface rendering (right panels). C) Cross-sections of the dorsal (left panels) and ventral (right
849 panels) part of the tongue stained against the full length Notch1 protein (green). Cell nuclei are
850 stained with DAPI (blue). Asterisks indicate the magnified areas in the corresponding region of
851 the overview. D) Cross-sections showing the dorsal (left panel) and ventral (right panel) parts of
852 the tongue of a *Notch1*^{CreERT}*:R26mTmG*$^{fl/fl}$ mouse. Both the dorsal and the ventral epithelium
853 express the Notch1-driven mGFP (green). Unrecombined tissue expresses *mTomato* (red). Cell
854 nuclei stained with DAPI (blue). Asterisks indicates magnified area in the corresponding region of
855 the overview. E) Cross-sections of the dorsal (left panel) and ventral (right panel) parts of the
856 tongue showing Jag1 staining (green). Cell nuclei are stained with DAPI (blue). F) Cross-sections
857 of the dorsal (left panel) and ventral (right panel) parts of the tongue showing Dll4 staining (green).
858 Nuclei are stained with DAPI (blue). Scale bars in overviews100µm. Scale bars in magnification
859 50µm.

860

861

862

863 **Figure 2: The Notch ligand Jagged1 and Dll4 expression is mutually exclusive in the early stage**
864 **of OSCC**

865 (A) Schematic representation of the tamoxifen induction and the 4NQO or DMSO treatment in 22-week-
866 old *Notch1CreERT:R26mTmGfl/fl* mice. (B) Cross-sections of the dorsal part of the tongue in DMSO-
867 treated (upper panels) and 4NQO-treated (lower panels) mice. mTomato expression (red) and mGFP
868 expression (green) in the healthy (DMSO) and aberrant (4NQO) epithelium of the tongue. Cell nuclei are
869 stained with DAPI (blue). (a-c) indicate the magnified areas in the corresponding regions of the overview
870 (a-c'). (C) Cross-sections of the dorsal part of the tongue stained against Dll4 (green) in DMSO- (upper
871 panels) and 4NQO-treated (lower panels) mice. Cell nuclei are stained with DAPI (blue). (D) Cross-sections
872 of the dorsal part of the tongue stained against Jag1 (green) in DMSO-treated (left panels) and 4NQO-
873 treated (right panels) mice. Cell nuclei are stained with DAPI (blue). Note the gradient of the Jag1 staining
874 in the 4NQO-treated epithelium: the epithelium distant from the lesion is Jag1-positive (red arrows), the
875 staining is reduced in the epithelium close to the hyperplasia (yellow arrows) and is absent in the
876 hyperplastic tissue (white arrows). The dotted line indicates the borders of the epithelial hyperplasia. (E)
877 Cross-sections of the dorsal part of the tongue showing Sox2 staining (green, upper panels), K5 (green,
878 middle panels) and K10 (green, lower panels) in the healthy (DMSO) and aberrant (4NQO) epithelium of
879 the tongue. Cell nuclei are stained with DAPI (blue). (d-i) indicate the magnified areas in the corresponding
880 regions of the overview (d'-i'). Scale bars in overviews100µm. Scale bars in magnification 50µm.

881

882

883 **Figure 3: Dll4 is specifically expressed in the OSCC exophytic outgrowth**

884 (A) Schematic representation of the 4NQO or DMSO treatment in 32-week-old *R26:mTomatofl/fl*
885 mice. B) Cross-sections of the dorsal part of the tongue in DMSO-treated (upper panels) and
886 4NQO-treated (lower panels) mice. *mTomato* expression (red) and *mGFP* expression (green) in
887 the healthy (DMSO) and aberrant (4NQO) epithelium of the tongue. Cell nuclei are stained with
888 DAPI (blue). Asterisks indicate the magnified areas in the corresponding regions of the overview.
889 (C) Cross-sections of the dorsal part of the tongue stained against Jag1(green) in DMSO- (left
890 panels) and 4NQO-treated (right panels) mice. Cell nuclei are stained with DAPI (blue). (D) Cross-
891 sections of the dorsal part of the tongue stained against Dll4 (green) in DMSO-treated (left panels)
892 and 4NQO-treated (right panels) mice. Cell nuclei are stained with DAPI (blue). The dotted line
893 indicates the borders of the OSCC overgrowth. Asterisks indicate the magnified areas in the
894 corresponding regions of the overview. Scale bars in overviews100µm. Scale bars in magnification
895 50µm.

896

897 **Figure 4: Transcriptome analysis of differential gene expression in the tongue epithelium of**
898 **4NQO-treated mice**

899 (A) Organoid formation assay using single epithelial stem cells derived from the tongue.
900 Treatment with CB103 inhibits organoid formation from single-cell suspensions, indicating
901 impaired stem cell function. Scale bar: 50 µm. (B) Schematic representation of the tongue's
902 epithelium separation for RNA extraction and follow up analysis. (C) qRT-PCR shows
903 upregulation of Dll4 expression and downregulation of Hey1 and Hey2 expression in 4NQO-
904 treated mice. Error bars indicate standard error. *=p<0.05; **=p<0.01; ***=p<0.001 (D) Gene Set

905 Enrichment Analysis (GSEA) plot for the Notch-signaling signature shows changes in the Notch
906 pathway in 4NQO condition when compared to DMSO. (E) Heatmap visualization of 2000
907 differentially expressed genes with hierarchical clustering. (F) Volcano plot confirm higher
908 expression of Dll4 in 4NQO over DMSO conditions. (G) Gene Set Enrichment Analysis (GSEA)
909 shows alterations in the process of keratinocytes differentiation and keratinization in 4NQO
910 condition. (H) GSEA identify alterations in the apical junction complex and EMT signatures (I)
911 Gene Ontology (GO) classification analysis for categories of biological processes (left panel) and
912 cellular components (right panel) comparing DMSO- versus 4NQO-treated epithelium. (L)
913 Volcano plot identified an increased expression of EMT markers Vimentin, ZEB1, ZEB2,
914 Tenascin C and Snail3. (M) qRT-PCR confirmation of EMT markers ZEB1 and ZEB2 upregulated
915 in 4NQO versus DMSO condition. Error bars indicate standard error. *=p<0.05; **=p<0.01;
916 ***=p<0.001

917

918 **Figure 5: Epithelial cells invade the tongue's mesenchyme in 4NQO-treated mice**

919 (A) Schematic representation of the 4NQO or DMSO treatment in 38-week-old *R26:mTomatofl/fl*
920 mice. (B) Cross-sections displaying the dorsal part of the tongue labelled with K14 (cyan) in
921 DMSO-treated (left panels) and 4NQO-treated mice (right panels). Background tissue expressed
922 *mTomato* (red). Asterisks indicate the magnified areas in the corresponding regions of the
923 overview. (C) Cross-sections displaying the dorsal part of the tongue labelled with P63 (cyan) in
924 DMSO-treated (left panels) and 4NQO-treated (right panels) mice. Background tissue expressed
925 *mTomato* (red). Asterisks indicate the magnified areas in the corresponding regions of the
926 overview. (D) Cross-sections of the dorsal part of the tongue stained with Snail (cyan) in DMSO-
927 treated (left panel) and 4NQO-treated condition (right panels) mice. Cell nuclei are stained with

928 DAPI (blue). Asterisk indicates the magnified area in the corresponding region of the overview.
929 White arrows indicate Snail-positive cells. (E) Cross-sections of the dorsal part of the tongue
930 stained with Vimentin (cyan) and E-cadherin (green) in DMSO-treated (left panel) and 4NQO-
931 treated (right panels) mice. Cell nuclei are stained with DAPI (blue). Asterisks indicate the
932 magnified areas in the corresponding regions of the overview. White arrows indicate sole Vimentin
933 staining, while yellow arrows indicate staining for both Vimentin and E-cadherin. Scale bars in
934 overviews 100µm. Scale bars in magnification 50µm.
935
936

937 **Figure 6: Detection of Notch1-expressing epithelial cells and their progeny within the**
938 **infiltrated mesenchyme of the tongue.**
939 (A) Schematic representation illustrating the tamoxifen induction and 4NQO or DMSO treatment
940 of 38-week-old *Notch1*^{CreER}*T:R26mTmG*$^{fl/fl}$ mice. (B) Cross-sections displaying the Notch1-driven
941 expression of *mGFP* in DMSO-treated epithelium. Unrecombined tissue expressed *mTomato*
942 (red). Cell nuclei are stained with DAPI (blue). Asterisk indicates the magnified area in the
943 corresponding region of the overview. (C) Tongue cross-sections displaying the Notch1-driven
944 expression of *mGFP* in 4NQO-treated mice after ten days of tamoxifen induction. Unrecombined
945 tissue expressed *mTomato* (red). Cell nuclei are stained with DAPI (blue). Asterisks indicate the
946 magnified areas in the corresponding regions of the overview. (D) Cross-sections displaying the
947 endogenous Notch1-full length expression (cyan) in the tongue epithelium of DMSO-treated (left
948 panels) and 4NQO-treated (right panels) mice. Unrecombined tissue expressed *mTomato* (red).
949 Asterisks indicate the magnified areas in the corresponding regions of the overview. (E) Cross-
950 sections showing the distribution of Dll4 (green) in the tongue epithelium of DMSO-treated (left
951 panels) and 4NQO-treated (right panels) mice. Asterisk indicates magnified area in the
952 corresponding region of the overview. Dashed lines indicate the extent of the epithelial infiltration
953 in the musculature of the tongue. Scale bars in overviews 100µm. Scale bars in magnification
954 50µm.
955
956
957
958

959 **Figure 7: Notch signaling in human squamous cell carcinoma**

960 (A) Histological examination of human healthy epithelium. Hematoxylin/Eosin staining is used to
961 identify the histological condition of the samples analyzed. Corresponding areas are then stained
962 for Dll4 (B) and Jag1(C). Overview of expression for Dll4 (upper panel) and magnifications (lower
963 panels). Scale bar in overview 500µm. Scale bar in magnification 50µm. (D) Histological
964 examination of human hyperplastic epithelium. Hematoxylin/Eosin staining is used to identify the
965 histological condition of the samples analyzed. Corresponding areas are then stained for Dll4 (E)
966 and Jag1(F). Overview of expression (upper panel) and magnifications (lower panels). Scale bar
967 in overview 500µm. Scale bar in magnification 50µm. (G) Histological examination of human
968 squamous cell carcinoma tissue. Hematoxylin/Eosin staining is used to identify aberrant histology
969 in two representative patients (Patient#1 with hyperplastic epithelium: middle panel, Patient#2
970 with squamous carcinoma: right panel). (H) Distribution of Dll4 in Patient#1 and Patient#2.
971 Magnified areas show expression of Dll4 protein. Scale bar in magnification: 100µm. Scale bar in
972 overview: 1mm. (I) Distribution of Jag1 protein in Patient#1 and Patient#2 in overview and
973 magnified areas. Scale bar in magnification: 100µm. Scale bar in overview: 1mm.

974

975 **Figure 8: CB103 treatment leads to broad transcriptional reprogramming in human**
976 **squamous cell carcinoma cells**

977 (A) Schematic overview of the experimental setup: SCC25 human squamous cell carcinoma cells
978 were treated with the pan-Notch inhibitor CB103 or DMSO (control) for five days prior to
979 downstream analyses. (B) qRT-PCR analysis shows that CB103 treatment significantly decreases
980 expression of the Notch ligand DLL4 and the stemness-associated markers SOX2 and P63. (C)
981 Bar plot summarizing Gene Ontology (GO) classification of cellular components, comparing gene

982 expression profiles between CB103- and DMSO-treated SCC25 cells.
983 (D) Heatmap with hierarchical clustering of the top 500 differentially expressed genes identified
984 via bulk RNA sequencing of SCC25 cells treated with CB103 or DMSO. (E) Gene Set Enrichment
985 Analysis (GSEA) plots show enrichment of keratinization (left) and keratinocyte differentiation
986 (right) signatures following CB103 treatment. (F) Volcano plot highlighting upregulation of
987 keratin genes (e.g., KRT1, KRT10) and downregulation of the stemness marker SOX2 after CB103
988 treatment.
989 (G) GSEA plot showing increased expression of genes involved in keratin filament organization
990 in CB103-treated cells. (H) GSEA plot illustrating changes in genes associated with cytoskeletal
991 components following CB103 exposure. (I) GSEA plot showing modulation of the epithelial-to-
992 mesenchymal transition (EMT) gene signature in response to CB103 treatment.
993
994 **Figure 9: Blockage of Notch transcription results in disruption of SCC cells migratory**
995 **activity**
996 A) Volcano plot showing upregulation of transcripts associated with desmosomes and cell
997 adhesion molecules in CB103-treated cells (e.g., plakoglobin (JUP), desmocollins (DSC1/2), and
998 desmogleins (DSG1/2). (B) GSEA plot highlighting enrichment of gene ontology cellular
999 components related to desmosomes in CB103- versus DMSO-treated conditions. (C) qRT-PCR
1000 analysis of SCC25 cells treated with DMSO or CB103 demonstrates increased expression of
1001 desmosomal structural components following Notch inhibition (e.g. desmoplakin (DSP),
1002 desmoglein 1 (DSG1), and desmocollins (DSC1 and DSC2)). (D) GSEA plot showing changes in
1003 apical junction-related gene signatures in SCC25 cells treated with CB103. (E) Representative
1004 immunofluorescence images of actin filaments and focal adhesions in SCC25 cells treated with

1005 DMSO or CB103. Green: phalloidin. Red: vinculin. Blue: DAPI. Scale bar: 10 µm. (F)
1006 Quantification of focal adhesion complexes per cell. *** $p < 0.001$. (G) Scratch wound assay of
1007 SCC25 cells treated with DMSO or CB103. Scale bar 100µm. (H) Quantification of the cell-free
1008 area in the scratch assay. Values normalized to the initial scratched area (day 0). Error bars
1009 represent standard error. **=$p<0.01$; ***=$p<0.001$; ****=$p<0.0001$ (I) Time-lapse imaging of
1010 SCC25 cells treated with DMSO or CB103, showing single frames from representative recordings
1011 over a 2-hour 25-minute period (related to Movies 3 and 4). Scale bar 50µm. (J) Quantification of
1012 single-cell displacement lengths using Imaris spot tracking.***=$p<0.001$
1013
1014

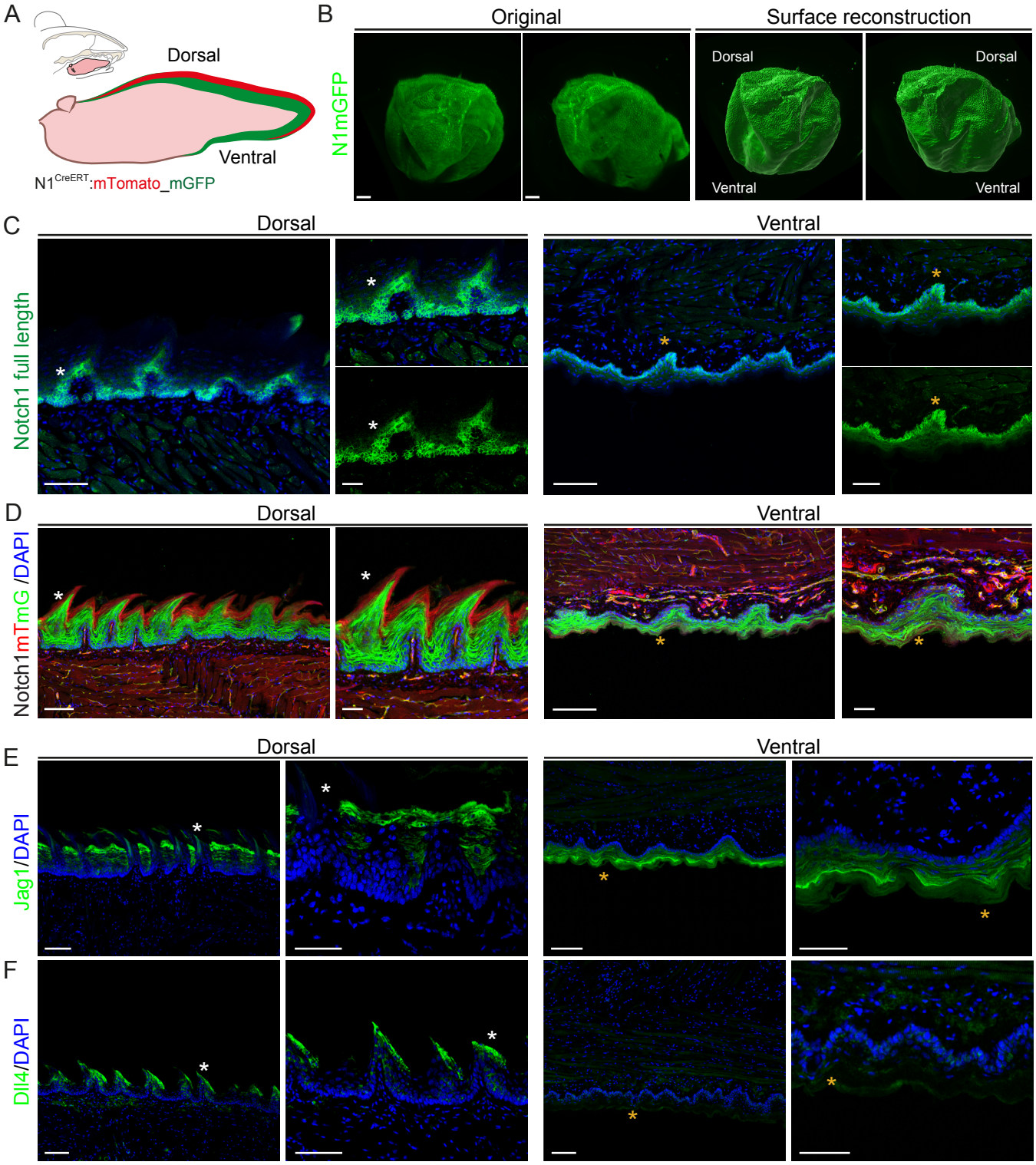
A
Dorsal
Ventral
N1CreERT:mTomato_mGFP
B
Original
Surface reconstruction
N1mGFP
Dorsal
Ventral
Dorsal
Ventral
C
Dorsal
Ventral
Notch1 full length
D
Dorsal
Ventral
Notch1mTmG /DAPI
E
Dorsal
Ventral
Jag1/DAPI
F
Dll4/DAPI

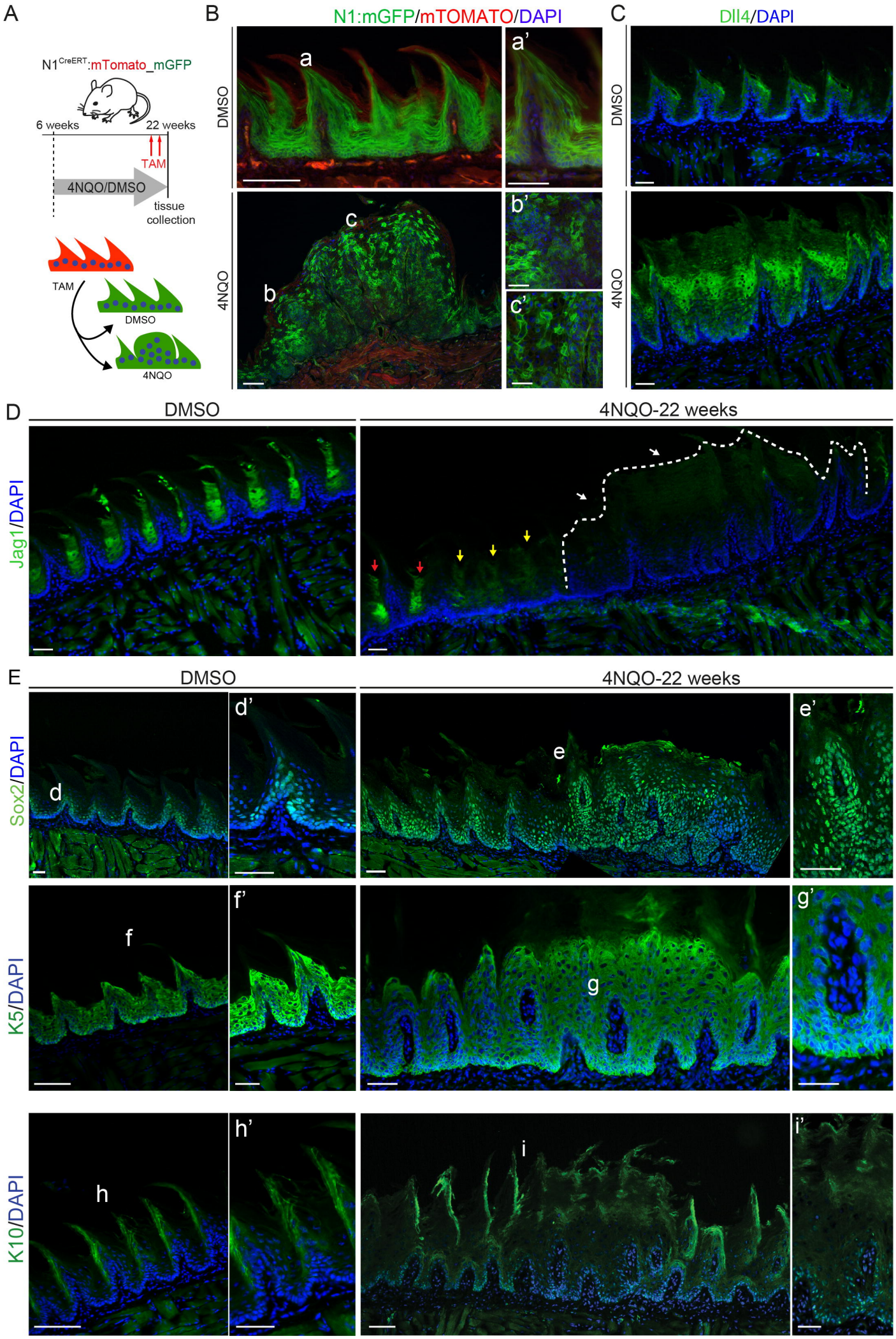
A
N1CreERT:mTomato_mGFP
6 weeks
22 weeks
TAM
4NQO/DMSO
tissue collection
TAM
DMSO
4NQO
B
N1:mGFP/mTOMATO/DAPI
DMSO
4NQO
a
a'
b
b'
c
c'
C
Dll4/DAPI
DMSO
4NQO
D
DMSO
4NQO-22 weeks
Jag1/DAPI
E
DMSO
4NQO-22 weeks
Sox2/DAPI
d
d'
e
e'
K5/DAPI
f
f'
g
g'
K10/DAPI
h
h'
i
i'

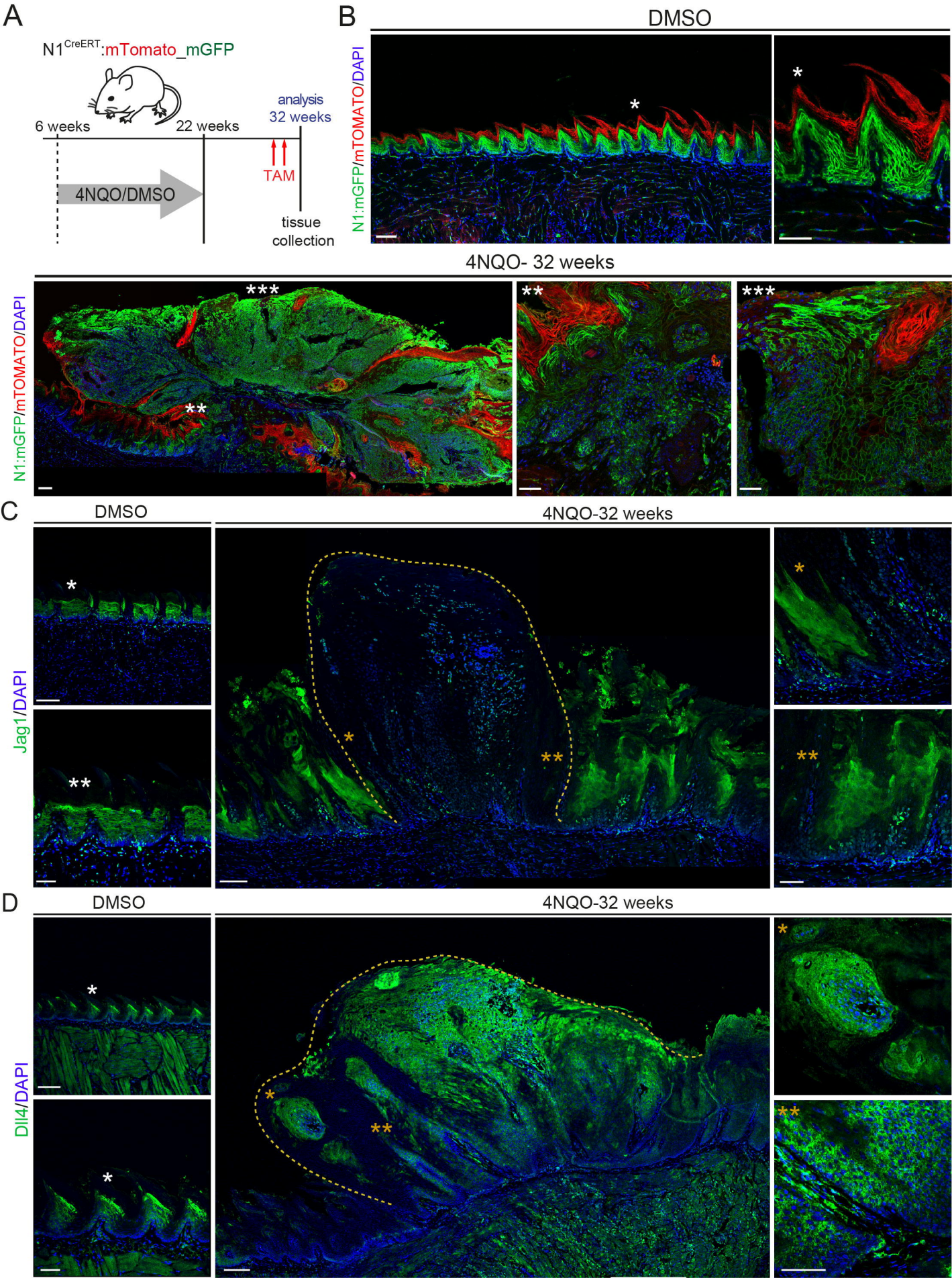
A
N1CreERT:mTomato_mGFP
6 weeks
22 weeks
analysis
32 weeks
TAM
4NQO/DMSO
tissue
collection
B
DMSO
N1:mGFP/mTOMATO/DAPI
4NQO- 32 weeks
N1:mGFP/mTOMATO/DAPI
C
DMSO
4NQO-32 weeks
Jag1/DAPI
D
DMSO
4NQO-32 weeks
Dll4/DAPI

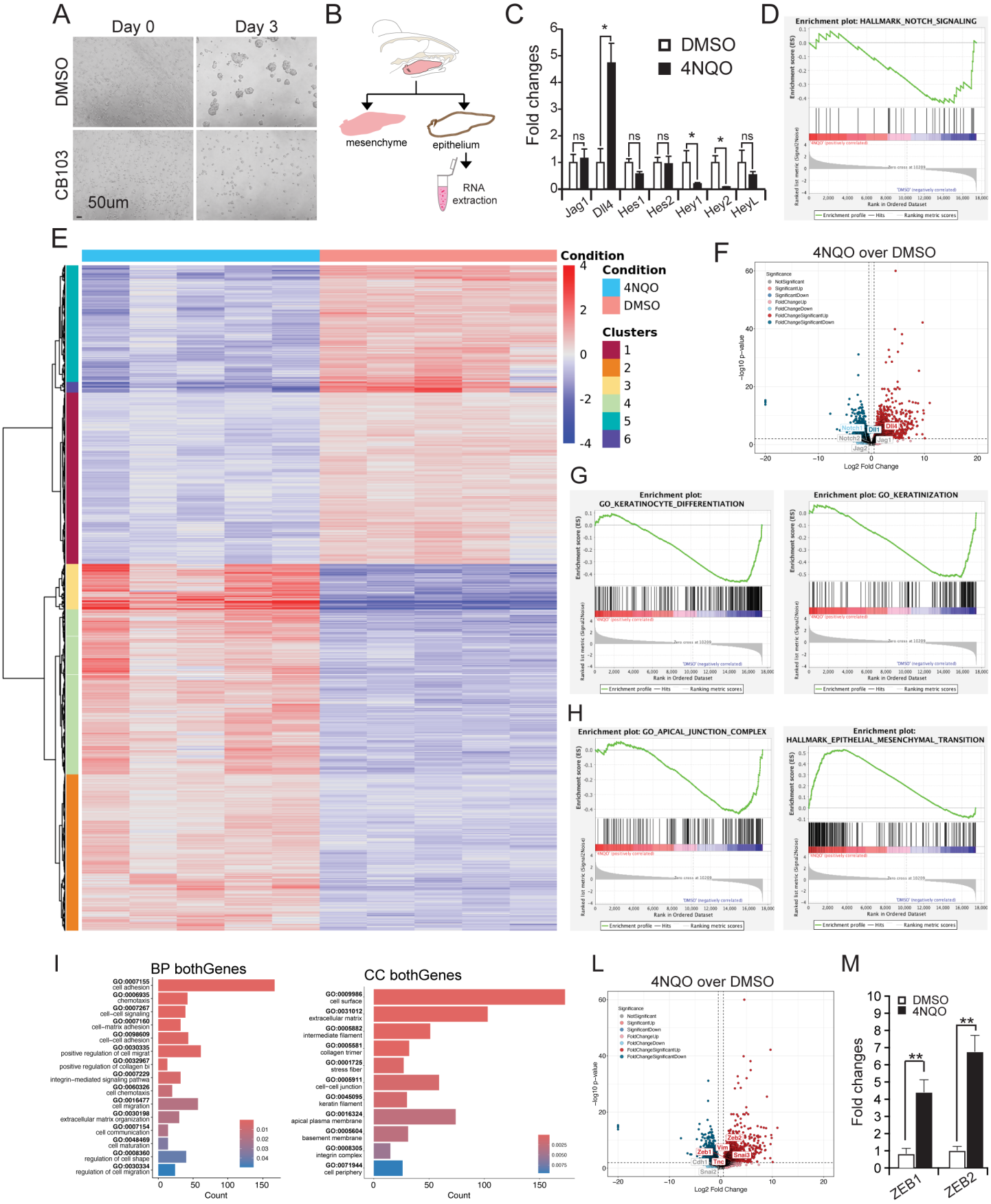
A
Day 0
Day 3
DMSO
CB103
50um
B
mesenchyme
epithelium
RNA extraction
C
Fold changes
DMSO
4NQO
ns
*
Jag1
Dll4
Hes1
Hes2
Hey1
Hey2
HeyL
D
Enrichment plot: HALLMARK_NOTCH_SIGNALING
E
Condition
4NQO
DMSO
Clusters
1
2
3
4
5
6
F
4NQO over DMSO
Significance
NotSignificant
SignificantUp
SignificantDown
FoldChangeUp
FoldChangeDown
FoldChangeSignificantUp
FoldChangeSignificantDown
-log10 p-value
Log2 Fold Change
Notch1
Dll1
Dll4
Notch2
Jag1
Jag2
G
Enrichment plot: GO_KERATINOCYTE_DIFFERENTIATION
Enrichment plot: GO_KERATINIZATION
H
Enrichment plot: GO_APICAL_JUNCTION_COMPLEX
Enrichment plot: HALLMARK_EPITHELIAL_MESENCHYMAL_TRANSITION
Enrichment score (ES)
Rank in Ordered Dataset
Enrichment profile
Hits
Ranking metric scores
I
BP bothGenes
GO:0007155 cell adhesion
GO:0006935 chemotaxis
GO:0007267 cell-cell signaling
GO:0007160 cell-matrix adhesion
GO:0098609 cell-cell adhesion
GO:0030335 positive regulation of cell migrat
GO:0032967 positive regulation of collagen bi
GO:0007229 integrin-mediated signaling pathwa
GO:0060326 cell chemotaxis
GO:0016477 cell migration
GO:0030198 extracellular matrix organization
GO:0007154 cell communication
GO:0048469 cell maturation
GO:0008360 regulation of cell shape
GO:0030334 regulation of cell migration
Count
CC bothGenes
GO:0009986 cell surface
GO:0031012 extracellular matrix
GO:0005882 intermediate filament
GO:0005581 collagen trimer
GO:0001725 stress fiber
GO:0005911 cell-cell junction
GO:0045095 keratin filament
GO:0016324 apical plasma membrane
GO:0005604 basement membrane
GO:0008305 integrin complex
GO:0071944 cell periphery
L
4NQO over DMSO
Zeb1
Vim
Zeb2
Snai1
Cdh1
Tnc
Snai2
M
Fold changes
DMSO
4NQO
**
ZEB1
ZEB2

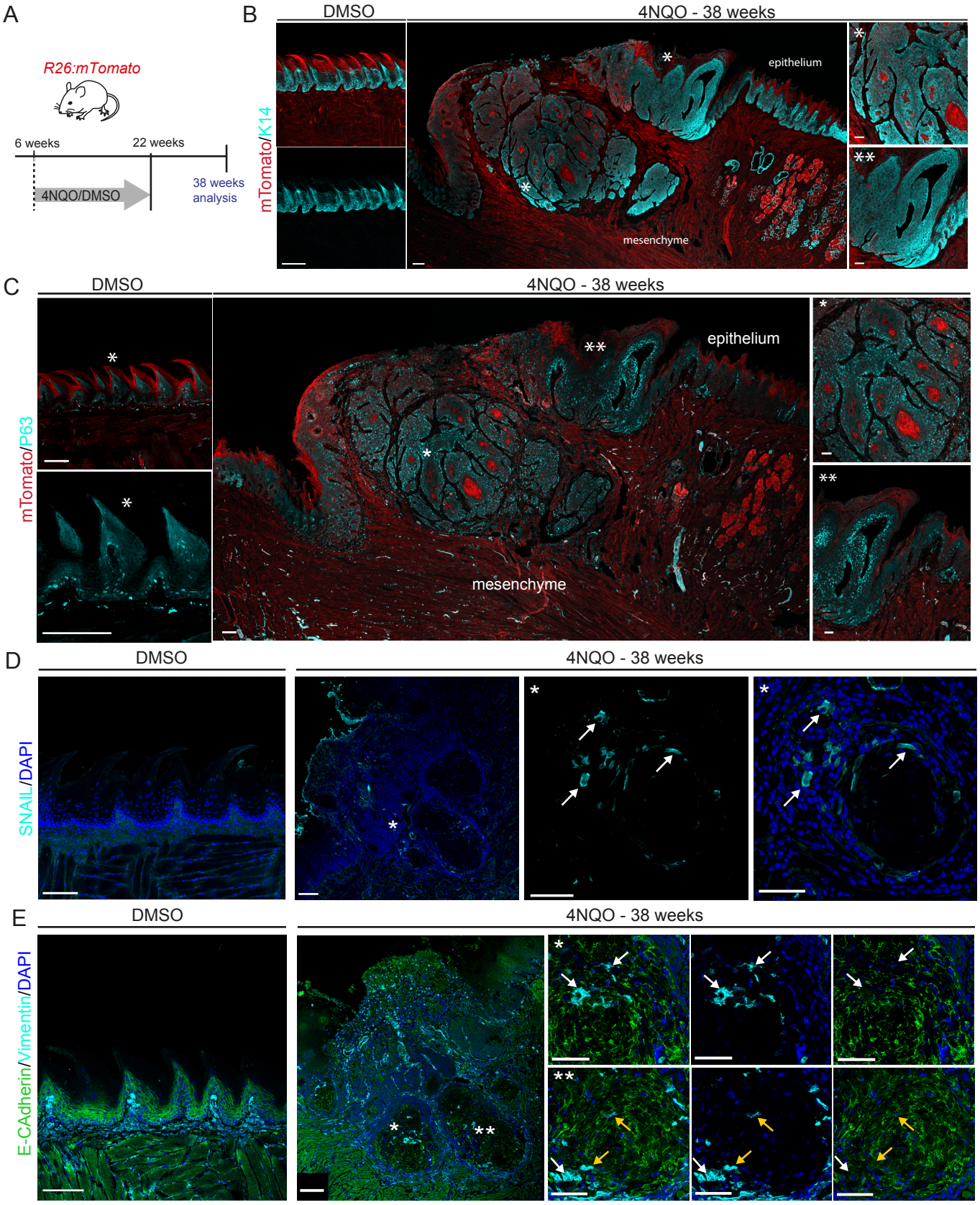
A
R26:mTomato
6 weeks
22 weeks
4NQO/DMSO
38 weeks analysis
B
DMSO
4NQO - 38 weeks
mTomato/K14
epithelium
mesenchyme
C
DMSO
4NQO - 38 weeks
mTomato/P63
epithelium
mesenchyme
D
DMSO
4NQO - 38 weeks
SNAIL/DAPI
E
DMSO
4NQO - 38 weeks
E-CAdherin/Vimentin/DAPI

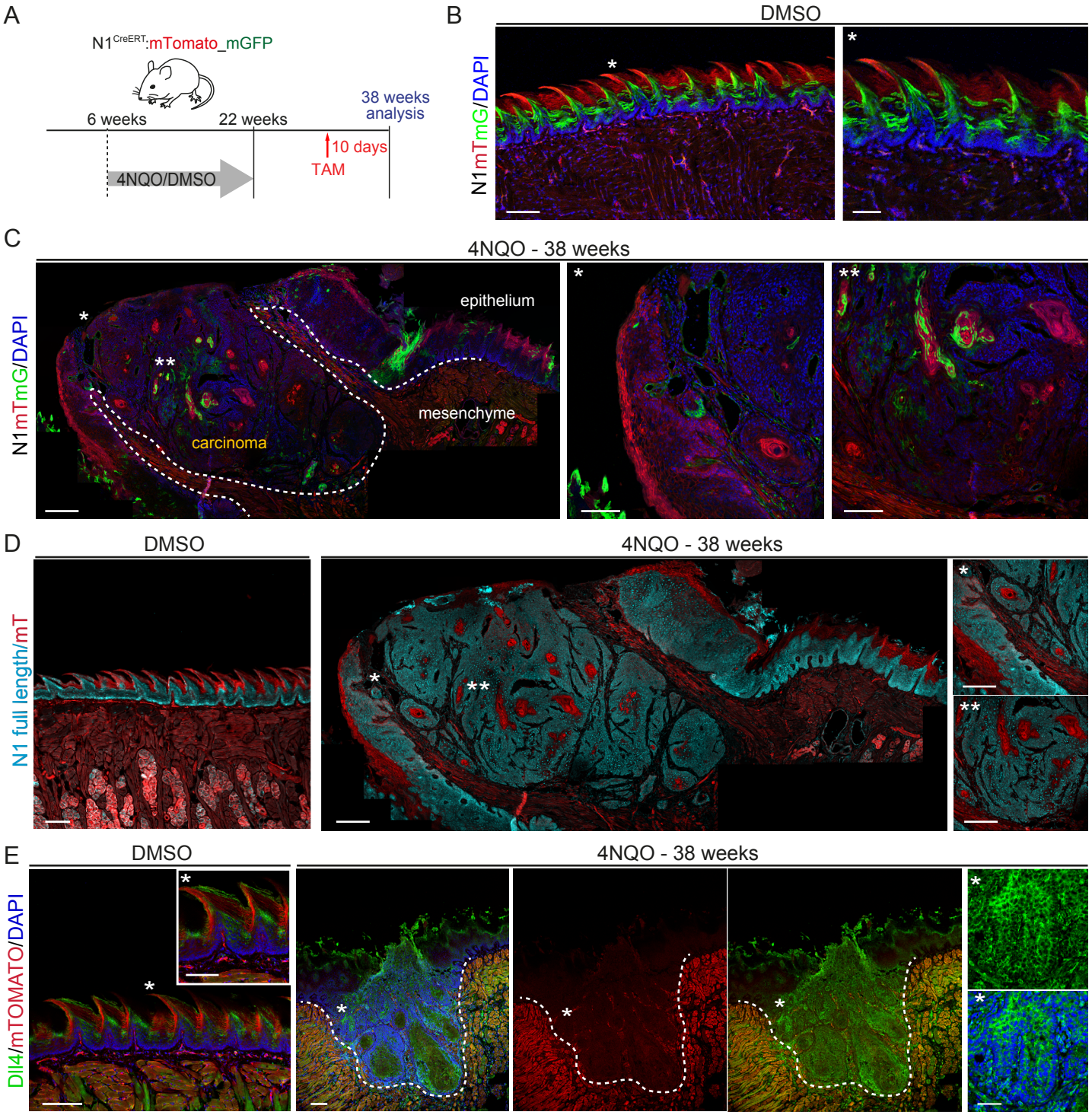
A
N1CreERT:mTomato_mGFP
6 weeks
22 weeks
38 weeks analysis
10 days
TAM
4NQO/DMSO
B
DMSO
N1mTmG/DAPI
C
4NQO - 38 weeks
N1mTmG/DAPI
epithelium
mesenchyme
carcinoma
D
DMSO
4NQO - 38 weeks
N1 full length/mT
E
DMSO
4NQO - 38 weeks
Dll4/mTOMATO/DAPI

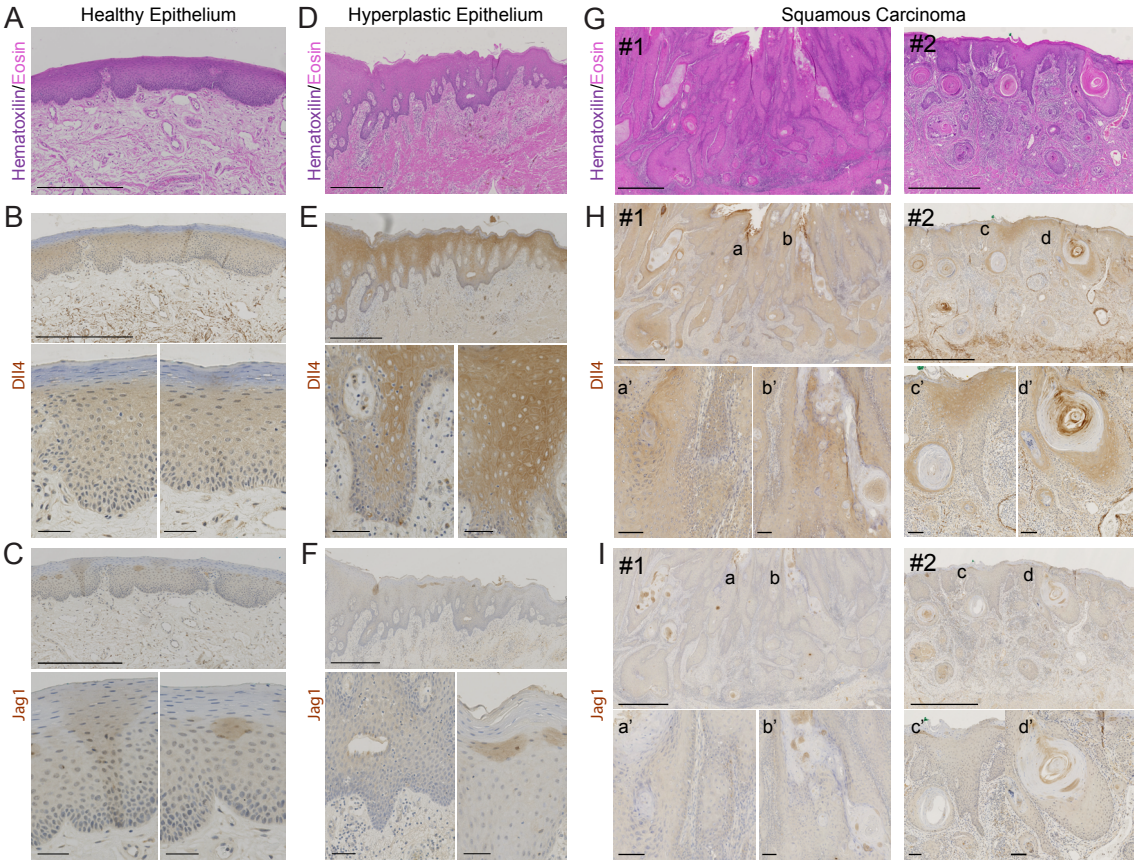
A
Healthy Epithelium
D
Hyperplastic Epithelium
G
Squamous Carcinoma
Hematoxilin/Eosin
#1
#2
B
E
H
Dll4
a
b
c
d
a'
b'
c'
d'
C
F
I
Jag1

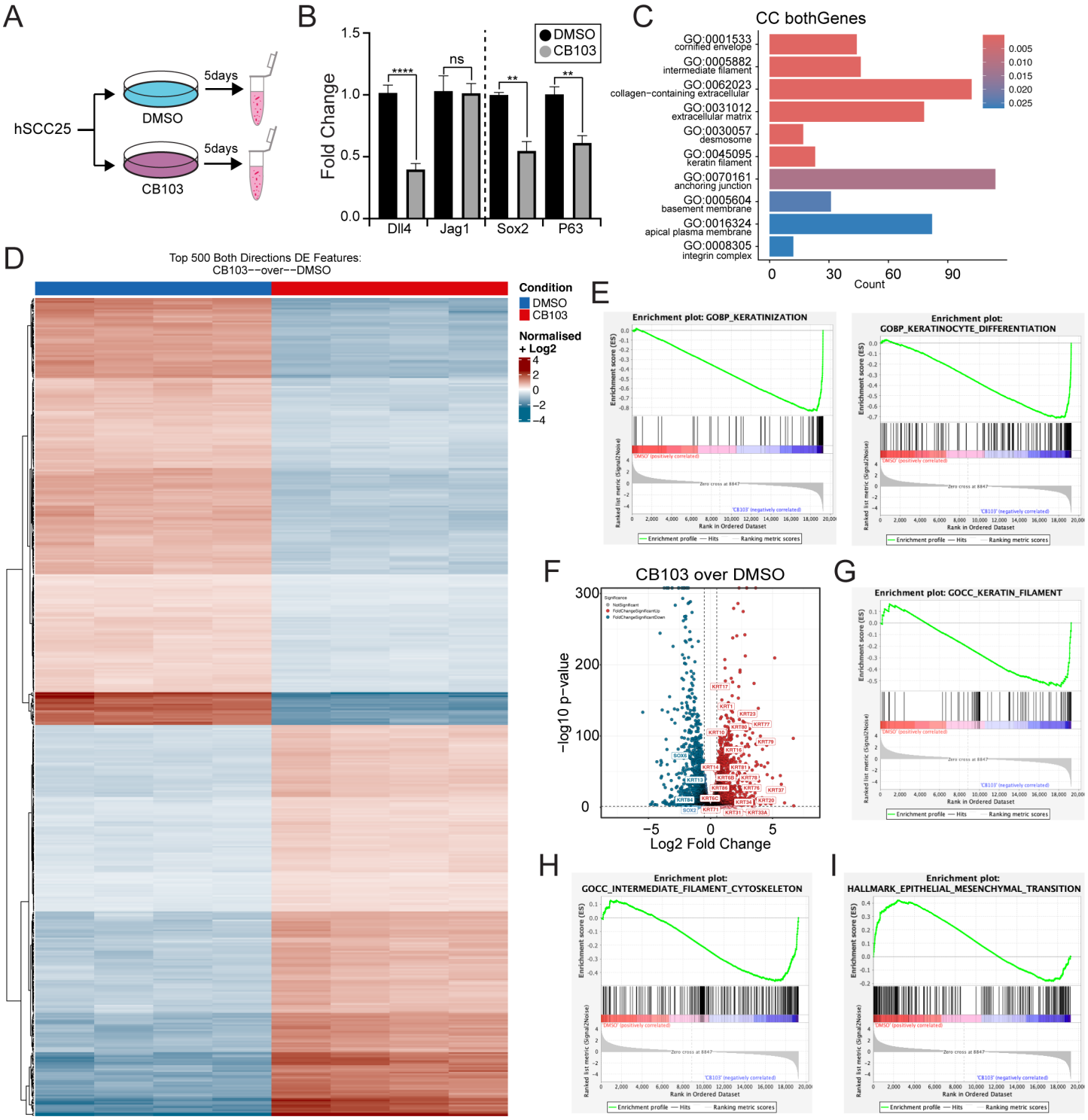
A
hSCC25
DMSO
CB103
5days
5days
B
DMSO
CB103
Fold Change
1.5
1.0
0.5
0.0
****
ns
**
**
Dll4
Jag1
Sox2
P63
C
CC bothGenes
GO:0001533 cornified envelope
GO:0005882 intermediate filament
GO:0062023 collagen−containing extracellular
GO:0031012 extracellular matrix
GO:0030057 desmosome
GO:0045095 keratin filament
GO:0070161 anchoring junction
GO:0005604 basement membrane
GO:0016324 apical plasma membrane
GO:0008305 integrin complex
0.005
0.010
0.015
0.020
0.025
0
30
60
90
Count
D
Top 500 Both Directions DE Features:
CB103−−over−−DMSO
Condition
DMSO
CB103
Normalised
+ Log2
4
2
0
−2
−4
E
Enrichment plot: GOBP_KERATINIZATION
Enrichment plot:
GOBP_KERATINOCYTE_DIFFERENTIATION
F
CB103 over DMSO
−log10 p−value
Log2 Fold Change
G
Enrichment plot: GOCC_KERATIN_FILAMENT
H
Enrichment plot:
GOCC_INTERMEDIATE_FILAMENT_CYTOSKELETON
I
Enrichment plot:
HALLMARK_EPITHELIAL_MESENCHYMAL_TRANSITION

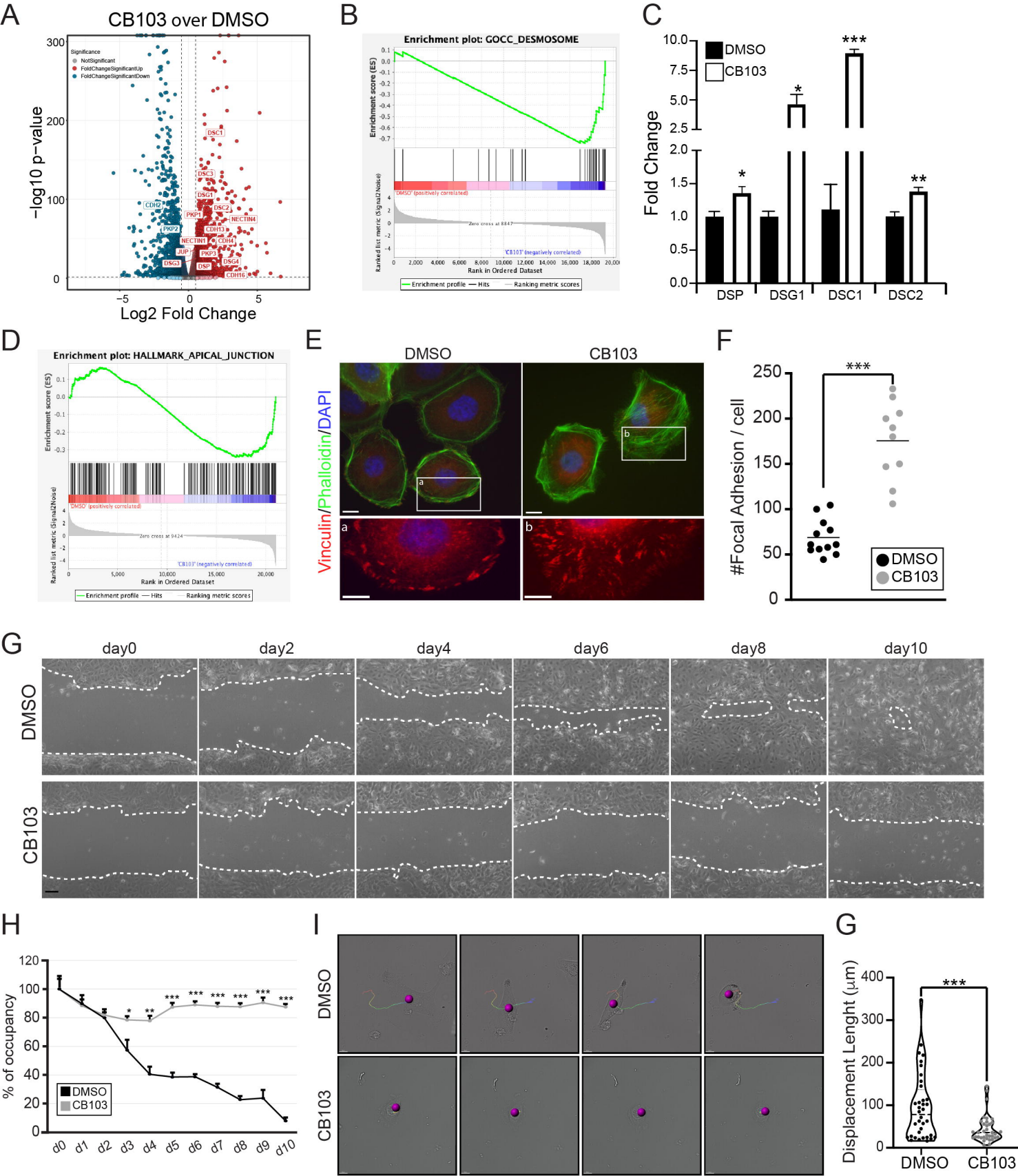
A
CB103 over DMSO
Significance
NotSignificant
FoldChangeSignificantUp
FoldChangeSignificantDown
−log10 p−value
Log2 Fold Change
DSC1
DSC3
DSG1
DSC2
CDH2
PKP1
NECTIN4
PKP2
CDH13
NECTIN1
CDH4
JUP
PKP3
DSG3
DSP
DSG4
CDH16
B
Enrichment plot: GOCC_DESMOSOME
Enrichment score (ES)
Ranked list metric (Signal2Noise)
'DMSO' (positively correlated)
Zero cross at 8847
'CB103' (negatively correlated)
Rank in Ordered Dataset
Enrichment profile
Hits
Ranking metric scores
C
DMSO
CB103
Fold Change
DSP
DSG1
DSC1
DSC2
D
Enrichment plot: HALLMARK_APICAL_JUNCTION
Enrichment score (ES)
Ranked list metric (Signal2Noise)
'DMSO' (positively correlated)
Zero cross at 9424
'CB103' (negatively correlated)
Rank in Ordered Dataset
Enrichment profile
Hits
Ranking metric scores
E
DMSO
CB103
Vinculin/Phalloidin/DAPI
F
#Focal Adhesion / cell
DMSO
CB103
G
day0
day2
day4
day6
day8
day10
DMSO
CB103
H
% of occupancy
DMSO
CB103
d0
d1
d2
d3
d4
d5
d6
d7
d8
d9
d10
I
DMSO
CB103
G
Displacement Lenght (μm)
DMSO
CB103